



HAL
open science

Equation of State of hcp Fe-C-Si Alloys and the Effect of C Incorporation Mechanism on the Density of hcp Fe alloys at 300 K 2

Martha G Pamato, Y Li, Daniele Antonangeli, F Miozzi, Guillaume Morard, I G Wood, Lidunka Vočadlo, J P Brodholt, M Mezouar

► To cite this version:

Martha G Pamato, Y Li, Daniele Antonangeli, F Miozzi, Guillaume Morard, et al.. Equation of State of hcp Fe-C-Si Alloys and the Effect of C Incorporation Mechanism on the Density of hcp Fe alloys at 300 K 2. *Journal of Geophysical Research*, In press. hal-02987201

HAL Id: hal-02987201

<https://hal.science/hal-02987201>

Submitted on 3 Nov 2020

HAL is a multi-disciplinary open access archive for the deposit and dissemination of scientific research documents, whether they are published or not. The documents may come from teaching and research institutions in France or abroad, or from public or private research centers.

L'archive ouverte pluridisciplinaire **HAL**, est destinée au dépôt et à la diffusion de documents scientifiques de niveau recherche, publiés ou non, émanant des établissements d'enseignement et de recherche français ou étrangers, des laboratoires publics ou privés.

Equation of State of *hcp* Fe-C-Si Alloys and the Effect of C Incorporation

Mechanism on the Density of *hcp* Fe alloys at 300 K

M.G. Pamato^{1,2*}, Y. Li¹, D. Antonangeli³, F. Miozzi^{3†}, G. Morard^{3,4}, I.G. Wood¹, L. Vočadlo¹, J.P. Brodholt¹, M. Mezouar⁵

¹ Department of Earth Sciences, University College London, Gower Street, London, WC1E 6BT, United Kingdom, ² Department of Geosciences, University of Padova, Via G. Gradenigo 6, 35131, Padova, Italy, ³ Sorbonne Université, Muséum National d' Histoire Naturelle, UMR CNRS 7590, Institut de Minéralogie, de Physique des Matériaux, et de Cosmochimie (IMPMC), 75005 Paris, France, ⁴ Univ. Grenoble Alpes, Univ. Savoie Mont Blanc, CNRS, IRD, IFSTTAR, ISTERre, 38000 Grenoble, France, ⁵ European Synchrotron Radiation Facility, Grenoble, France

*Corresponding author: Martha G. Pamato (martha.pamato@unipd.it)

† Current address: Dipartimento di Scienze della Terra, Università degli Studi di Milano, via Mangiagalli 34, 20133 Milano, Italy.

Key Points:

- Synchrotron X-ray diffraction and density functional theory calculations were performed on *hcp* Fe-C-Si alloy with 4 at% C and 3 at% Si
- Different incorporation mechanisms were examined and the *hcp* Fe-C-Si alloy sample takes the interstitial form
- Assuming a wrong incorporation mechanism leads to incorrect density determination and a more enhanced density contrast between the alloy and pure Fe.

23 **Abstract**

24 Si and C are cosmochemically abundant elements soluble in *hcp* Fe under pressure and
25 temperature, and could therefore be present in the Earth's inner core. While recent *ab initio*
26 calculations suggest that the observed inner core density and velocities could be matched by an
27 Fe-C-Si alloy, the combined effect of these two elements has only recently started to be
28 investigated experimentally. We therefore carried out synchrotron X-ray diffraction
29 measurements of an *hcp* Fe-C-Si alloy with 4 at% C and 3 at% Si, up to ~ 150 GPa. Density
30 functional theory calculations were also performed to examine different incorporation
31 mechanisms. These calculations suggest interstitial C to be more stable than substitutional C
32 below ~ 350 GPa. In our calculations, we also find that the lowest energy incorporation
33 mechanism in the investigated pressure range (60-400 GPa) is one where two C atoms occupy
34 one atomic site; however this is unlikely to be stable at high temperatures. Notably, substitutional
35 C is observed to decrease the volume of the *hcp* Fe, while interstitial C increases it. This allows
36 us to use experimental and theoretical equations-of-state to show unambiguously that C in the
37 experimental *hcp* Fe-C-Si alloys is not substitutional, as is often assumed. This is crucial since
38 assuming an incorrect incorporation mechanism in experiments, leads to incorrect density
39 determinations of $\sim 4\%$, undermining attempts to estimate the concentration of C in the inner
40 core. In addition, the agreement between our experiments and calculations, support Si and C as
41 being light elements in the inner core.

42 **1 Introduction**

43 The only direct investigation of the inaccessible Earth's deep interior is provided by
44 seismological studies of sound wave velocities through the Earth. The comparison between
45 seismological observations and elastic properties of candidate materials at the relevant conditions
46 present in the deep Earth, allows to relate geophysical data with the chemistry and temperature of

47 the Earth's interior. In the Earth's mantle, mineralogical and compositional models can match
48 the observed velocities to approximately 1% (e.g. Irifune et al., 2008; Murakami et al., 2012;
49 Bass & Zhang, 2015; Pamato et al., 2016; Kurnosov et al., 2017). Conversely, for the inner core,
50 sound wave velocities of pure Fe or Fe-Ni alloys in the *hcp* structure usually obtained from
51 mineral physics are much higher (10–30 %) than those from seismic observations (Vočadlo,
52 2007; Belonoshko et al., 2007; Martorell, Brodholt, et al., 2013). Numerous arguments were
53 proposed over the years to explain these discrepancies, including, for example, large
54 compositional effects, pervasive partial melting, anelasticity or the stabilization of *bcc* Fe
55 (Vočadlo, 2007; Belonoshko et al., 2003, 2007, 2017, 2019; Antonangeli et al., 2004).

56
57 Theoretical calculations have shown that the sound velocities observed in the inner core could be
58 matched by *hcp* Fe due to a strong non linear softening of the elastic properties at 360 GPa above
59 7000 K (Martorell, Vočadlo, et al., 2013). However, even though the velocities of the inner core
60 were matched by pure Fe, the density remained too high (by 2–3%) to agree with geophysical
61 observations, and so lighter elements are still needed to explain this density mismatch.
62 Furthermore, the suggested pre-melting softening is generally suppressed in iron alloys (e.g.
63 Martorell et al., 2016). With the exception of Fe_7C_3 (Chen et al., 2014; Prescher et al., 2015), all
64 the iron compounds examined so far exhibit higher velocities than those found in the core. For
65 the case of Fe_7C_3 , a strong non linear softening has been also observed (Li et al., 2016), but,
66 while the calculated velocities agree with seismic data, the density is far too low (by $\sim 8\%$).
67 Many recent computational and experimental studies addressing core compositions point to the
68 need of two or more distinct light elements (e.g. Badro et al. 2104; Morard, Nakajima, et al.,
69 2017; Li et al. 2018; Edmund et al., 2019). However, the identity of this light element mixture is

70 still largely debated. Very recently Li et al. (2018), reported *ab initio* molecular dynamics
71 (AIMD) calculations which reveal the observed inner-core density and sound velocities can be
72 simultaneously matched by a range of ternary and quaternary Fe alloys, all containing carbon.
73 This constrains possible solid solution's space in a multiple light elements model explaining all
74 of the major seismic constraints. However, even when limiting the discussion to mineral physics
75 properties, several aspects still remain uncertain, including the different incorporation
76 mechanisms of C in Fe and its effect on seismic properties. From density functional theory
77 (DFT) calculations, Huang et al. (2005) suggested that C takes the substitutional form in *hcp* Fe
78 at 0 K above approximately 300 GPa, as confirmed by Li et al. (2019) who, using *ab initio*
79 molecular dynamics, also found that C takes the substitutional form at 360 GPa and 6500 K.
80 However, at lower pressures, interstitial C and other complex defect structures may be stabilized
81 (Huang et al., 2005; Caracas, 2017; Li et al., 2019). In fact, the thermodynamic model of Fei &
82 Brosh (2014), based on experiments at pressures <20 GPa, and more recently the work by Yang
83 et al. (2019) indicate that the interstitial form is preferred up to inner-core pressures. The change
84 of incorporation mechanism may be related to the variance of solubility. Lord et al. (2009), for
85 example, found a negligible C solubility in *hcp* Fe approaching 50 GPa. However, more recently,
86 Mashino et al. (2019) performed melting experiments up to 255 GPa and predicted a solubility of
87 1 wt.% in *hcp* Fe at inner-core boundary conditions. A question remains as to whether different
88 incorporation mechanisms of C in iron have an effect on the seismic properties of an Fe-C alloy;
89 does it matter if the carbon is on an interstitial, substitutional or other site within the *hcp* crystal
90 structure?

91

92 Multiple lines of evidence, from geochemical and cosmochemical arguments (e.g. Allègre et al.,
93 1995), to core formation models based on metal-silicate partitioning (e.g. Siebert et al., 2013;
94 Fischer et al., 2015), to isotopic considerations (e.g. Fitoussi et al., 2009; Shahar et al., 2009),
95 support silicon to be present in the core. Due to the almost equal Si partitioning between liquid
96 and *hcp* iron (Alfè et al., 2002), the quantity of Si present in the inner core is not significantly
97 different from that expected for the liquid core. However, many recent studies point out that Si is
98 very unlikely to be the only light element in the core (Badro et al., 2014; Morard, Andraut, et al.,
99 2017) and specifically in the inner core (Martorell et al., 2016; Antonangeli et al., 2018; Edmund
100 et al., 2019). An alloy in the ternary Fe-C-Si system thus seems to provide the simplest
101 composition possibly accounting for the bulk of geophysical and geochemical evidences of the
102 inner core. In particular, very recent AIMD calculations (Li et al., 2018) indicate that an *hcp*
103 $\text{Fe}_{60}\text{C}_2\text{Si}_2$ alloy is expected to have density, compressional and shear sound velocities matching
104 those of PREM at 360 GPa for simulation temperatures between 6000 and 7000 K.

105

106 To confirm this prediction, both high-pressure experiments and further simulations need to be
107 performed to clarify the effects of C on the seismic properties of Fe and Fe-Si alloys over a wider
108 range of pressures and temperatures. Thus, here we address the effect of the C incorporation
109 mechanism on density by combining synchrotron X-ray diffraction (XRD) measurements on an
110 *hcp* Fe-C-Si alloy (with 4 at % C and 3 at % Si at 300 K and up to ~ 150 GPa), with DFT
111 calculations. In particular, we examined the different incorporation mechanisms of carbon in the
112 structure of the alloy as a function of pressure. Our results are then used to discuss the density of
113 a Fe-C-Si alloy at inner core conditions.

114 **2 Materials and Methods**

115 **2.1 Experiments**

116 The starting material, with a nominal composition of Fe 93 at%, C 4 at%, Si 3 at%, was
117 synthesised by an ultra-rapid quench method at the ICMPE (Institut de Chimie et des Matériaux
118 de Paris-Est, Paris, France) using nominally pure Fe (Neyco F-12734), Si (Wacker) and Fe₃C
119 (Neyco FC-76857/1). Homogeneous Fe-alloys, in the form of ribbons, approximately 25 μm
120 thick and of 20-30 mm width, were synthesized following the procedure described in Morard et
121 al. (2011).

122
123 The chemical composition of the synthesized alloys was measured by means of a Cameca SX100
124 electron microprobe analyser equipped with a cold finger and an O₂ flux at Camparis center-
125 Sorbonne Université. The resulting composition for the alloy is 3 (±0.2) at% Si, 4 (±0.4) at% C
126 and 93 (±0.06) at% Fe (Fe₉₃C₄Si₃). In addition, scanning electron microscopy (SEM) analyses
127 were performed on the sample using a Zeiss Ultra 55 scanning electron microscope installed at
128 the IMPMC (Institut de Minéralogie, de Physique des Matériaux et de Cosmochimie),
129 confirming homogeneity at the micron scale (Miozzi, Morard, et al., 2020).

130
131 Samples were prepared for the high-pressure experiments by crushing parts of a ribbon specimen
132 and compressing it between two diamonds (~ 600 μm culet), in order to obtain the desired
133 thickness (usually between 5 and 10 microns). The sample was then loaded in a rhenium gasket
134 of 20 μm thickness, with a hole of 60 μm, with 100/300 μm bevelled anvils. High pressures were
135 generated using a Le Toullec-type (membrane driven) diamond anvil cell. Tungsten carbide seats
136 designed for diamonds with conical support were used (Boehler & De Hantsetters, 2004). The
137 sample was loaded alongside Mo as a pressure calibrant, with Ne acting as the pressure

138 transmitting medium; - the equation of state parameters for the Mo pressure calibrant were taken
139 to be: $V_0 = 31.14 \text{ \AA}^3$ (Litasov et al., 2013; Ross & Hume-Rothery, 1963), $K_0 = 260(1) \text{ GPa}$ and K'
140 $= 4.19(5)$.

141
142 Angle-dispersive XRD measurements were carried out at the ID27 beamline of the European
143 Synchrotron Radiation Facility in Grenoble (Mezouar et al., 2005). In the experiments, a
144 monochromatic beam of 33 keV ($\lambda = 0.3738 \text{ \AA}$) was focused on an area $< 3 \times 3 \text{ \mu m}^2$ (full width at
145 half maximum). Data collection times were typically between 10 and 30 s; diffraction patterns
146 were collected on a MAR CCD detector at pressures between 48 and 150 GPa at 300 K.

147
148 2-D diffraction images were integrated using the software DIOPTAS (Prescher & Prakapenka,
149 2015), using calibration parameters (sample detector distance and orientation) derived from the
150 diffraction pattern of a cerium dioxide (CeO_2) standard. Diffraction patterns were indexed with
151 PD Indexer (http://pmsl.planet.sci.kobe148u.ac.jp/~seto/?page_id=20). The sample started to
152 transform from the *bcc* structure stable at ambient pressure to the *hcp* structure at $\sim 19 \text{ GPa}$. All
153 *bcc* reflections were absent by $\sim 22 \text{ GPa}$. At least five sample diffraction lines are clearly
154 observed for the *hcp* phase over the entire pressure range. However, the diffraction patterns are,
155 to some extent, non-ideal in terms of randomness of the distribution (both 101 and 102
156 reflections showed intensity variation around the powder ring). Also, the 002 reflection, while
157 present over the entire pressure range, is very weak, due to a small preferential orientation, likely
158 induced by sample thinning before loading. Therefore, it was not possible to perform full profile
159 data refinements. The unit-cell parameters were thus calculated from the *d*-spacings of the
160 reflections 100, 101, 102, and 110 using the software Unit Cell by Holland & Redfern (1997).

2.2 DFT Calculations

DFT calculations were performed by using a $4 \times 4 \times 2$ *hcp* supercell, the VASP code (Kresse & Joubert, 1999) and PAW potential (Blöchl, 1994). The valence states $3p^63d^64s^2$, $3s^23p^2$ and $2s^22p^2$ were adopted for Fe, Si and C, respectively. We employed the generalised gradient approximation (GGA); the Perdew-Wang (Perdew & Wang, 1992) exchange-correlation functional was used. We adopted the ordered symmetrical structure for the alloy by placing solid solution atoms with the maximum sum of distances between them to achieve homogeneous dispersion. The octahedral interstitial site was adopted for the interstitial carbon atoms as the tetrahedral interstitial site was reported to be less favourable (Caracas, 2017). A plane-wave cutoff energy of 400 eV and 12 irreducible k-points were used to converge the results.

3 Results and Discussion

3.1 Equations of state

The diffraction pattern of the investigated alloy collected at 140 GPa (the upper end of the pressure range investigated) and indexed as hexagonal closed packed (*hcp*) iron, is shown in Figure 1.

Measured unit-cell volumes of *hcp* $\text{Fe}_{93}\text{C}_4\text{Si}_3$ alloy are presented in Figure 2 and show a smooth, continuous trend with increasing pressure, indicating the absence of any phase transition within the pressure range investigated.

The P – V data, reported in Table S1, were fitted using a third-order Birch–Murnaghan equation of state (BM3 EoS; Birch, 1947) with the software EosFit7 (Angel et al., 2014). All the parameters were refined resulting in the following EoS parameters: $V_0 = 22.7(2) \text{ \AA}^3$, $K_0 = 148(18) \text{ GPa}$, and $K_0' = 5.8(4)$ (Table 1). The EoS parameters are usually defined at 0 GPa (e.g., V_0 , K_0 and K_0').

185 However, as iron alloys in the *hcp*-structure are not stable and cannot be quenched at room
186 pressure and temperature, the EoS parameters can be defined at any other pressure in order to
187 compare different EoS in the pressure stability field of *hcp*-phases. The parameters refined
188 relative to a pressure scale from 50 GPa are: $V_{P=50} = 18.80(1) \text{ \AA}^3$, $K_{P=50} = 394(6) \text{ GPa}$, and K'
189 $_{P=50} = 4.8(2)$.

190

191 The measured unit-cell volumes of $\text{Fe}_{93}\text{C}_4\text{Si}_3$ are larger than those of pure *hcp* Fe, Fe-Si, and Fe-
192 C alloys reported in the literature (Figure 2a). If compared to the pure *hcp* Fe EoS as determined
193 by Dewaele et al. (2006), the P-V trend established here shows a different curvature, with the
194 difference in the volumes increasing at high pressure, thus highlighting a difference in
195 compressibility. On the other hand, differences are less pronounced when compared to recent
196 EoS of pure *hcp* Fe reported by Sakai et al. (2014), Yang et al. (2019) and Miozzi, Matas, et al.
197 (2020). Specifically, the new data on the $\text{Fe}_{93}\text{C}_4\text{Si}_3$ alloy determined here, show a compressibility
198 curve comparable to the more recent results for pure *hcp* Fe, but with higher volumes.

199 **3.2 Comparison of Fe-C-Si alloys**

200 A comprehensive comparison of the equations of state parameters K_0 and K_0' of the different
201 alloys considered here is illustrated in the inset in Figure 2a. The data published by Dewaele et
202 al. (2006), Sakai et al. (2014), Yang et al. (2019) and Miozzi, Matas, et al. (2020) for pure Fe and
203 by Edmund et al. (2019) and Yang et al. (2019) for Fe-Si and Fe-C alloys, respectively, were
204 reevaluated in order to obtain the variance-covariance matrixes (Angel, 2000) and to construct
205 the confidence ellipses (Table 1, Inset Figure 2a). The confidence ellipses of our dataset are
206 larger than those reported in the literature. This might be due to the different pressure and
207 volume uncertainties, how these are taken into account in the analysis, and to the number and

208 range of measured pressure points in the different studies. Here, both pressure and volume
209 uncertainties were weighted, whereas most of the studies from the literature report an equally-
210 weighted fit. When performing an equally-weighted fit, errors are smaller and thus also the
211 correlation between K_0 and K_0' is smaller. In addition, given the trade-off between V_0 , K_0 and K_0' ,
212 it is important to measure the volume of the *hcp* structure at the lowest pressure in order to
213 constrain the refinement of the room temperature EoS (see e.g., Miozzi, Matas, et al. (2020)). In
214 our study, due to the lack of low-pressure points (we report P - V data from 48 GPa, see Table S1)
215 the EoS refinement provides a less robust constraint of the reference volume at $P = 0$ (i.e. V_0).

216 The ellipse representing our data and the one of Yang et al. (2019) for pure Fe intersect at the
217 68.3% confidence level. Our data are also in good agreement with the recent EoS of Fe reported
218 by Miozzi, Matas, et al. (2020), which extends the data set to lower pressures, and also, within
219 experimental error, with that of Sakai et al. (2014). The confidence ellipses are in fact parallel
220 and the error bars intersect. All this indicates that the value of the isothermal room pressure bulk
221 modulus obtained in this study for $\text{Fe}_{93}\text{C}_4\text{Si}_3$ is very similar to the values obtained for pure Fe
222 from Sakai et al (2014), Yang et al (2019) and Miozzi, Matas, et al. (2020). A critical review of
223 the EoS parameters of pure Fe is beyond the aim of this paper. It is important to note, however,
224 that the confidence ellipse built with the K_0 and K_0' values of Miozzi, Matas, et al. (2020)
225 intersects only with that of Sakai et al. (2014) for pure Fe, while, that of Dewaele et al. (2006)
226 does not intersect with our results and also does not intersect with other results in the literature
227 for pure Fe, as a direct consequence of the different compressibility already mentioned.

228

229 Edmund et al. (2019), recently suggested that *hcp* Fe can contain up to 5 wt% Si (approximately
230 8 at%) without any significant change of the unit cell volume (Figure 2a). As shown by both

231 compression curve and the confidence ellipses, in fact, the data by Edmund et al. (2019) are in
232 good agreement with the data from Dewaele et al. (2006) for *hcp* Fe. Yang et al. (2019) reported
233 that the incorporation of C has a direct effect on the volume of *hcp* Fe. In particular, their fitting
234 results showed that addition of C to Fe leads to larger unit cell volumes at the same pressure,
235 with the magnitude of the increase remaining constant up to ~135 GPa, the highest investigated
236 pressure, with compression curves almost parallel. The authors fitted a BM3 EoS with K_0' fixed
237 to 4.79 (value taken from Fei et al., 2016 for pure Fe) to systematically compare the EoS
238 parameters for pure Fe, Fe-0.31 wt% C (~1.4 at% C), and Fe-1.37 wt% C (~6.1 at% C).
239 However, when the data of Yang et al. (2019) are fitted without constraining K_0' , the resulting
240 magnitude of the volume increase is not the same. Furthermore, it can be seen that extrapolation
241 of the EoS established for Fe-6.1 at% C and Fe-1.4 at% C crosses above 120 GPa, with the
242 volumes of the first becoming smaller than the second and approaching the volume of pure Fe
243 (Figure 2b). Even when limiting comparison to the directly investigated pressure range, we note
244 that Fe-6.1 at% C has smaller volumes than the sample studied here, which contains less C (4
245 at% C), and volumes similar to those of Fe-Si alloy with 8 at% Si (Edmund et al. 2019) and pure
246 Fe by Dewaele et al. (2006). Moreover, as shown in the inset in Figure 2a, the confidence
247 ellipses representing our data and those of Yang et al. (2019) on pure Fe and Fe-1.4 at % C
248 intersect, indicating a shift only in V_0 without changing the compressibility, while that of Fe-6.1
249 at. %C is closer to those of Fe-8 at% Si (Edmund et al. 2019) and pure Fe according to Dewaele
250 et al. (2006).

251 **3.3 Effect of the incorporation mechanism of carbon on the compressibility of *hcp*** 252 **Fe**

253 While Si is incorporated via substitution in iron without introducing major changes in the volume
254 (Edmund et al., 2019), the strong effect of small amounts of C on the volume of *hcp* Fe may well

255 be related to its interstitial position in the *hcp* structure (Caracas, 2017; Yang et al., 2019).
256 Impurities, such as C, in a solid can be present as substitutional or interstitial atoms. In addition,
257 impurities can develop defect clusters, possibly modifying the physical and mechanical properties
258 of the material (Smidt & Sprague, 1972; Li et al., 2017; Li et al., 2019) including its volume and
259 its compressibility. Therefore, it is essential to address the different incorporation mechanisms of
260 carbon in the structure of the alloy at different pressures, to evaluate their relevance in defining
261 the properties of the Earth's core. To this end, in our *ab initio* calculations, we considered both
262 binary Fe-C and ternary Fe-C-Si alloys. At first we relaxed the structures and calculated
263 enthalpies for the binary substitutional Fe_{62}C_2 , interstitial Fe_{64}C_2 and dimer Fe_{63}C_2 (two C at one
264 atomic site) alloys (see the structural illustration in Figure S1). Then, we also calculated volumes
265 and fitted the EoS of pure Fe, $\text{Fe}_{60}\text{C}_2\text{Si}_2$ via substitution, $\text{Fe}_{62}\text{C}_2\text{Si}_2$ via interstitial carbon and
266 $\text{Fe}_{61}\text{C}_2\text{Si}_2$ with a dimer (Table S2 and Table 1, respectively). The composition of the calculated
267 alloys corresponds to Fe \sim 3 at% C and \sim 3 at% Si.

268
269 Calculations using a 16 Fe atoms supercell (Huang et al. 2005) support a transition from
270 interstitial to substitutional C at pressure of \sim 300 GPa at 0 K. At high temperature, calculations
271 based on the quasiharmonic approximation (QHA) (Li et al. 2019) showed that the substitutional
272 alloy is more stable than the interstitial one at 360 GPa and 6500 K, confirming that the
273 temperature effect does not significantly vary the relative stability (at least at inner core
274 pressures). They also showed that the inclusion of C as a dimer is more stable than both
275 substitutional and interstitial alloying at 360 GPa and 0 K, but entropy does not favour the dimer
276 and it becomes less stable than substitutional C at 6500 K (Li et al., 2019). The enthalpies of C in
277 different forms calculated at 0 K in this study are shown as a function of pressure in Figure 3.

278 The enthalpy calculations show that interstitial C is more stable than substitutional C below
279 ~350 GPa. The difference in transition pressure with Huang et al. (2005) may be due to the size
280 effect and concentration dependence. The dimer is shown to be more stable than both the
281 substitutional and interstitial forms at all examined pressures from 60 to 400 GPa. However, on
282 qualitative grounds, considering the temperature effect and entropy cost in forming the dimer,
283 this could become unfavourable at high temperatures. Quantitative high-temperature calculations
284 will be necessary to determine at what temperature the dimer structure becomes unstable, but, in
285 any case, it definitely has its own stability field over a large pressure range extending to a certain
286 temperature. Overall, these theoretical studies show that the interstitial alloy is more stable at low
287 pressures, while the substitutional defect is more stable at 360 GPa. This also implies that a
288 change of C incorporation mechanism is likely under inner-core conditions.

289
290 The calculated volumes of the alloys considered, together with those that we measured
291 experimentally, at different pressures are displayed in Figure 4.

292 Substitutional C decreases the volume of the *hcp* unit cell relative to that of pure Fe, while
293 interstitial C increases it. The dimer also increases the volume of *hcp* Fe but to a much lesser
294 degree than the interstitial defect. Calculated and experimentally determined volumes are in
295 excellent agreement at pressures above ~60 GPa, suggesting that C in the experimental sample is
296 interstitial.

297 At lower pressures (below 60 GPa) the calculated volumes are smaller than those determined
298 experimentally. This difference is attributed to the approximations in the theoretical approach.
299 DFT may fail to capture the correct electron correlation at low pressures, becoming more reliable
300 at high pressures as a consequence of the increased delocalization of the electrons This mismatch

301 between calculations and experiments at low pressures has also been observed for *hcp* Fe (Figure
302 5).

303 Actually, in the case of pure Fe the difference in volumes is much more pronounced, with the
304 experimental and computational results starting to agree closely only at ~ 200 GPa.

305 To better understand the effect of C and the incorporation mechanism, Figure 6 shows the
306 pressure dependence of the volume difference $\Delta V = V - V_{\text{Fe}}$ (where V is the unit-cell volume of the
307 alloy and V_{Fe} is the reference unit-cell volume for *hcp* Fe) for *hcp* Fe and Fe-Si-C alloys. The
308 experimental volumes for $\text{Fe}_{93}\text{C}_4\text{Si}_3$ are compared to the different experimental V_{Fe} available in
309 the literature, whereas the calculated volumes are compared to *hcp* Fe from our DFT simulations.
310 Regardless of the reference V_{Fe} used, we can unambiguously confirm that C in the experimental
311 sample is not substitutional as the ΔV for substitutional C is negative. In the pressure range of the
312 experiments (50-150 GPa), the experimental volume differences are close, although slightly
313 higher, to those reported for the dimer configuration, whereas at pressures above 200 GPa, all
314 (except when using the EoS of Miozzi, Matas, et al., 2020) approach the ΔV expected for
315 interstitial C. Once considering the different EoS of *hcp* Fe and the differences among the
316 experiments (pressure scales, hydrostaticity, etc) and possible problems with the calculations at
317 low pressures, this analysis seems to suggest that C in the experimental sample is interstitial. The
318 more stable dimer might be present in some domains at lower pressures. Possibly the sample
319 synthesis process at ambient pressure and high temperature favored interstitial carbon. Dimer
320 formation in the quenched samples might then be entropically unfavorable or prevented by
321 kinetic barriers and slow diffusion of vacancies.

322 Previous computational studies (Huang et al., 2005; Caracas, 2017; Li et al., 2019) suggest that C
323 preferentially occupies the octahedral interstitial site at low pressure. The presence of C slightly

324 expands the octahedron containing the impurity, resulting in an increase in unit cell volume
325 (Figure 2 and 4). According to Caracas (2017), the volume increase is almost linear with the
326 amount of C and is approximately independent of pressure within the stability field of the *hcp*
327 phase (see their Figure 2). In agreement with Caracas (2017), the volume increase is almost
328 linear with C content, from 1.4 at% (Yang et al. 2019) to 4 at% C (this study) and almost
329 independent of pressure. Contrarily to the other datasets, Fe-6.1 at% C by Yang et al. (2019)
330 seems not to follow the same trend; above ~80 GPa the volume ratio decreases as a function of
331 pressure and is much lower than that expected on the basis of the other data for lower C contents,
332 and below that calculated by Caracas (2017) for a similar composition (Figure S2). These data by
333 Yang et al (2019) also disagree with the EoS predicted for a similar composition (Fe-6 at% C) by
334 Huang et al. (2005) and, therefore, it appears that Fe-6.1at% C by Yang et al. (2019) may not be
335 an interstitial solid solution.

336
337 To summarise, even a small amount of C in the alloy has a strong effect on the volume of *hcp* Fe.
338 Calculated and experimentally determined volumes are in excellent agreement at pressures above
339 ~60 GPa, suggesting that C in the experimental sample is interstitial. While substitutional C
340 decreases the volume of the *hcp* unit cell, interstitial C increases it. The inclusion of C as a
341 dimer, predicted by calculations to be the most stable, also increases the volume of *hcp* Fe, but to
342 a lesser degree than the interstitial defect.

343 **3.4 Effect of the incorporation mechanism of carbon on the density**

344 The effect of C on the density of *hcp* Fe is critical to estimation of the effect of C on the physical
345 properties of the Earth's inner core. A common practice in mineral physics is to calculate the
346 density of the alloy assuming a substitutional solid solution, which is valid, for example, for an

347 Fe-Si alloys as Si only enters in the *hcp* structure as a substitutional impurity. In this way, the
 348 density of a substitutional alloy $\mathbf{A}_{1-x}\mathbf{B}_x^{\text{S}}$ (s denotes substitutional) is calculated as follows:

$$349 \quad \rho = N \cdot [(1-x) \cdot \mathbf{M}_A + x \cdot \mathbf{M}_B] / V \quad (\text{eq. 1})$$

350 where N is the number of atoms in unit cell, V is the volume of unit cell. \mathbf{M}_A , \mathbf{M}_B are the molar
 351 mass for A, B and x is the molar fraction.

352 However, this is not directly applicable for other alloys like Fe-C, as C can have other solid
 353 solution mechanisms, such as incorporation interstitially. Following the established approach for
 354 *fcc* Fe-C alloys reported for example in Waseda et al. (2011), the density of an interstitial solid
 355 solution $\mathbf{A}_{1-x}\mathbf{B}_x^{\text{i}}$, (i denotes interstitial) in this case, is calculated as follows:

$$356 \quad \rho = N \cdot \left[\mathbf{M}_A + \frac{x}{1-x} \mathbf{M}_B \right] / V \quad (\text{eq. 2})$$

357 where the number N of atoms in unit cell in *hcp* Fe is two while in *fcc* is four.

358 The density in the case of the dimer defect, with two C atoms sitting at one lattice site, can be
 359 computed as a combination of one substitutional and one interstitial C.

360 In this study, the density of Fe-C-Si alloy considering Si as substitutional and C as interstitial
 361 $\mathbf{A}_{1-x-y}\mathbf{B}_x^{\text{S}}\mathbf{C}_y^{\text{i}}$, is calculated as follow:

$$362 \quad \rho = N \cdot \left[\left(\frac{1-x-y}{1-y} \right) \cdot \mathbf{M}_A + \frac{x}{1-y} \cdot \mathbf{M}_B + \frac{y}{1-y} \mathbf{M}_C \right] / V \quad (\text{eq. 3})$$

363 while if both Si and C are substitutional, the density for $\mathbf{A}_{1-x-y}\mathbf{B}_x^{\text{S}}\mathbf{C}_y^{\text{S}}$ is simply:

$$364 \quad \rho = N \cdot [(1-x-y) \cdot \mathbf{M}_A + x \cdot \mathbf{M}_B + y \cdot \mathbf{M}_C] / V \quad (\text{eq. 4})$$

365 Further details of density calculations of the Fe-C-Si alloy considering Si as substitutional and C
366 both as interstitial and as substitutional are reported in the supplementary material. The derived
367 density evolution for *hcp* Fe-C-Si with pressure is shown in Figure 7.

368
369 The density of the alloy experimentally determined in this study, with 4 at% C, is ~6.5 % smaller
370 than that of pure Fe when C is assumed to be substitutional, whereas it is only is ~2.5 % smaller
371 when C is assumed to be interstitial, roughly independent of pressure. Density calculations
372 assuming the interstitial incorporation mechanism are in remarkable agreement with DFT
373 calculations also showing a density reduction with added interstitial C in the Fe structure
374 (Caracas, 2017; Li et al., 2018). Caracas (2017) indicated that 1 wt.% (~4.5 at%) C would
375 decrease *hcp* Fe density by approximately 2.8%.

376
377 Yang et al. (2019) reported the density of Fe-1.37 wt % C (~6.1 at% C) to be 5.6% smaller than
378 the of pure *hcp* Fe. These authors state that interstitial C in the *hcp* structure enhanced the density
379 difference between pure Fe and the alloy. However, although the authors clearly assume C as
380 interstitial, the densities they report (see their Figure 2) were calculated assuming substitutional
381 solid solution (see our Figure 7). When the densities are calculated starting from the reported
382 volumes using the equation for interstitial carbon, C, the resulting values are anomalously large,
383 even larger than those of pure Fe (see Figure 7). As already discussed, it appears that the Fe-1.37
384 wt. % C studied by Yang et al. (2019) might not be an interstitial solid solution.

385
386 The correct interpretation of the incorporation mechanism is essential for evaluating the identity
387 and amount of light element(s) in the Earth's core. As reported above, the incorporation

388 mechanism affects both the volume and the mass of the unit cell. Substitutional C lowers the
389 volume of the *hcp* unit cell while the interstitial and, to a lesser degree, the dimer mechanisms
390 increase it (Figure 4 and 6). At the same time, the interstitial mechanism increases the mass
391 while the substitutional mechanism reduces it. The two effects act to cancel each other out when
392 calculating density. In fact, as shown by our DFT simulations, in which both the changes in unit-
393 cell volume and unit-cell contents are taken into account in an internally consistent way, the
394 density difference between a substitutional, interstitial and dimer alloy is almost negligible
395 (Figure 8).

396

397 This is different in the case of the experiments, in which the volume is directly measured,
398 without any prior assumption of C distribution. However, assumptions of the effective mass of
399 the unit-cell have to be made to derive density from the measured volumes. As illustrated in
400 Figure 8, the way this is done might lead to very different densities with very dissimilar
401 conclusions concerning the amount of light elements required to account for PREM values. In
402 particular, if the volume measured in the experiments is due to an interstitial mechanism but is
403 interpreted as being substitutional, the resulting density will be significantly lower, and a much
404 smaller concentration of light element would be required to match PREM. These results indicate
405 that it is vital to know the exact incorporation mechanism of the alloy and its effect on the elastic
406 properties with changing pressure and temperature, to correctly interpret the properties of the
407 inner core. To this end, the combination of experiments and theoretical studies provide unique
408 capabilities.

409

410 **4 Conclusions**

411 We have carried out volume and density measurements on an *hcp* Fe-C-Si alloy with 4 at% C
412 and 3 at% Si up to ~150 GPa, using a combination of synchrotron powder diffraction and DFT
413 simulations, carried out at the same pressure conditions, to facilitate interpretation of the
414 experiments and to validate the theoretical approach. In particular *hcp* Fe-C-Si alloys with a
415 different incorporation mechanism - substitutional, interstitial, and dimer - were examined to
416 precisely address the effect of C on the physical properties of the alloy.

417

418 Enthalpy calculations suggest that interstitial C is more stable than substitutional C below ~350
419 GPa. While the dimer, with two C atoms replacing an Fe atom, is more stable than both the
420 interstitial and substitutional C, it is destabilized by temperature and, at ambient temperature, it
421 can be kinetically inhibited by a diffusion barrier. Indeed, we find that C in the experimentally
422 investigated *hcp* Fe-C-Si alloy sample takes the interstitial form, as supported by the very good
423 agreement at pressure above ~60 GPa between the experimentally determined compression curve
424 and that obtained from calculations for the interstitial alloy. Calculated values for density in the
425 literature are often determined assuming a substitutional solid solution. However, this is not
426 applicable for an interstitial-type solid solution, such as that reported here. Assuming the wrong
427 incorporation mechanism when estimating density from measured volumes can lead to incorrect
428 density determination, resulting in a more enhanced density contrast between the alloy and pure
429 Fe. In turn, this can affect density-velocities systematics (Birch's law) resulting in erroneous
430 interpretation of inner core composition. Finally, the agreement between our experiments and
431 calculations, supports previous work (Li et al., 2018) suggesting Si and C combined can account
432 for core densities and velocities.

433

434 **Acknowledgments**

435 The authors thank Jeroen Jacobs (ESRF) for his assistance with the diamond anvil cell
436 preparation. M.G.P. received funding from the European Union's Horizon 2020 research and
437 innovation programme under the Marie Skłodowska-Curie grant agreement No 796755. This
438 project has received funding from NERC (grant NE/M015181/1 to L.V.) and from the European
439 Research Council (ERC) under the European Union's Horizon 2020 research and innovation
440 programme (Grant agreement No. 72460 to D.A.). Data will be available at the repository of
441 University of Padova (<http://researchdata.cab.unipd.it/385/>).

442

443 **References**

- 444 Alfè, D., Gillan, M. J., & Price, G. D. (2002). Composition and temperature of the earth's core
445 constrained by combining ab initio calculations and seismic data. *Earth and Planetary
446 Science Letters*. [https://doi.org/10.1016/S0012-821X\(01\)00568-4](https://doi.org/10.1016/S0012-821X(01)00568-4)
- 447 Allègre, C. J., Poirier, J. ., Humler, E., & Hofmann, A. W. (1995). The chemical composition of
448 the Earth. *Earth and Planetary Science Letters*. [https://doi.org/10.1016/0012-
449 821X\(95\)00123-T](https://doi.org/10.1016/0012-821X(95)00123-T)
- 450 Angel, R. J. (2000). Equations of State. *Reviews in Mineralogy and Geochemistry*, 41(1), 35–59.
451 <https://doi.org/10.2138/rmg.2000.41.2>
- 452 Angel, R. J., Gonzalez-Platas, J., & Alvaro, M. (2014). EosFit7c and a Fortran module (library)
453 for equation of state calculations. *Zeitschrift Fur Kristallographie*, 229(5), 405–419.
454 <https://doi.org/10.1515/zkri-2013-1711>
- 455 Antonangeli, D., Occelli, F., Requardt, H., Badro, J., Fiquet, G., & Krisch, M. (2004). Elastic
456 anisotropy in textured hcp-iron to 112 GPa from sound wave propagation measurements.
457 *Earth and Planetary Science Letters*, 225(1–2), 243–251.
458 <https://doi.org/10.1016/j.epsl.2004.06.004>
- 459 Antonangeli, D., Morard, G., Paolasini, L., Garbarino, G., Murphy, C. A., Edmund, E., et al.
460 (2018). Sound velocities and density measurements of solid hcp-Fe and hcp-Fe–Si (9 wt.%)
461 alloy at high pressure: Constraints on the Si abundance in the Earth's inner core. *Earth and
462 Planetary Science Letters*, 482, 446–453. <https://doi.org/10.1016/j.epsl.2017.11.043>
- 463 Badro, J., Côté, A. S., & Brodholt, J. P. (2014). A seismologically consistent compositional
464 model of Earth's core. *Proceedings of the National Academy of Sciences of the United
465 States of America*. <https://doi.org/10.1073/pnas.1316708111>
- 466 Belonoshko, A. B., Ahuja, R., & Johansson, B. (2003). Stability of the body-centred-cubic phase
467 of iron in the Earth's inner core. *Nature*, 424, 1032–1034.

- 468 <https://doi.org/10.1038/nature01954>
- 469 Belonoshko, A. B., Skorodumova, N. V., Davis, S., Osipov, A. N., Rosengren, A., &
470 Johansson, B. (2007). Origin of the Low Rigidity of the Earth's Inner Core. *Science*,
471 *316*(5831), 1603–1605. <https://doi.org/10.1126/science.1141374>
- 472 Belonoshko, A. B., Lukinov, T., Fu, J., Zhao, J., Davis, S., & Simak, S. I. (2017). Stabilization of
473 body-centred cubic iron under inner-core conditions. *Nature Geoscience*, *10*, 312–316.
474 <https://doi.org/10.1038/ngeo2892>
- 475 Belonoshko, A. B., Fu, J., Bryk, T., Simak, S. I., & Mattesini, M. (2019). Low viscosity of the
476 Earth's inner core. *Nature Communications*, *10*, 2483. [https://doi.org/10.1038/s41467-019-](https://doi.org/10.1038/s41467-019-10346-2)
477 [10346-2](https://doi.org/10.1038/s41467-019-10346-2)
- 478 Birch, F. (1947). Finite elastic strain of cubic crystals. *Physical Review*.
479 <https://doi.org/10.1103/PhysRev.71.809>
- 480 Blöchl, P. E. (1994). Projector augmented-wave method. *Physical Review B*.
481 <https://doi.org/10.1103/PhysRevB.50.17953>
- 482 Boehler, R., & De Hantsetters, K. (2004). New anvil designs in diamond-cells. *High Pressure*
483 *Research*. <https://doi.org/10.1080/08957950412331323924>
- 484 Buchen, J., Marquardt, H., Speziale, S., Kawazoe, T., Boffa Ballaran, T., & Kurnosov, A.
485 (2018). High-pressure single-crystal elasticity of wadsleyite and the seismic signature of
486 water in the shallow transition zone. *Earth and Planetary Science Letters*.
487 <https://doi.org/10.1016/j.epsl.2018.06.027>
- 488 Caracas, R. (2017). The influence of carbon on the seismic properties of solid iron. *Geophysical*
489 *Research Letters*, *44*(1), 128–134. <https://doi.org/10.1002/2016GL071109>
- 490 Chen, B., Li, Z., Zhang, D., Liu, J., Hu, M. Y., Zhao, J., et al. (2014). Hidden carbon in Earth's
491 inner core revealed by shear softening in dense Fe₇C₃. *Proceedings of the National*
492 *Academy of Sciences*, *111*(50), 17755–17758. <https://doi.org/10.1073/pnas.1411154111>
- 493 Dewaele, A., Loubeyre, P., Occelli, F., Mezouar, M., Dorogokupets, P. I., & Torrent, M. (2006).
494 Quasihydrostatic equation of state of Iron above 2 Mbar. *Physical Review Letters*, *97*(21),
495 29–32. <https://doi.org/10.1103/PhysRevLett.97.215504>
- 496 Edmund, E., Antonangeli, D., Decremps, F., Miozzi, F., Morard, G., Boulard, E., et al. (2019).
497 Velocity-Density Systematics of Fe-5wt%Si: Constraints on Si Content in the Earth's Inner
498 Core. *Journal of Geophysical Research: Solid Earth*, *124*(4), 3436–3447.
499 <https://doi.org/10.1029/2018JB016904>
- 500 Fei, Y., & Brosh, E. (2014). Experimental study and thermodynamic calculations of phase
501 relations in the Fe-C system at high pressure. *Earth and Planetary Science Letters*, *408*,
502 155–162. <https://doi.org/10.1016/j.epsl.2014.09.044>
- 503 Fei, Y., Murphy, C., Shibazaki, Y., Shahar, A., & Huang, H. (2016). Thermal equation of state of
504 hcp-iron: Constraint on the density deficit of Earth's solid inner core. *Geophysical Research*
505 *Letters*. <https://doi.org/10.1002/2016GL069456>
- 506 Fischer, R. A., Nakajima, Y., Campbell, A. J., Frost, D. J., Harries, D., Langenhorst, F., et al.
507 (2015). High pressure metal-silicate partitioning of Ni, Co, V, Cr, Si, and O. *Geochimica et*

508 *Cosmochimica Acta*. <https://doi.org/10.1016/j.gca.2015.06.026>

509 Fitoussi, C., Bourdon, B., Kleine, T., Oberli, F., & Reynolds, B. C. (2009). Si isotope
510 systematics of meteorites and terrestrial peridotites: implications for Mg/Si fractionation in
511 the solar nebula and for Si in the Earth's core. *Earth and Planetary Science Letters*.
512 <https://doi.org/10.1016/j.epsl.2009.07.038>

513 Holland, T. J. B., & Redfern, S. A. T. (1997). UNITCELL: A nonlinear least-squares program
514 for cell-parameter refinement implementing regression and deletion diagnostics. *Journal of*
515 *Applied Crystallography*. <https://doi.org/10.1107/S0021889896011673>

516 Huang, L., Skorodumova, N. V., Belonoshko, A. B., Johansson, B., & Ahuja, R. (2005). Carbon
517 in iron phases under high pressure. *Geophysical Research Letters*, 32.
518 <https://doi.org/doi:10.1029/2005GL024187>

519 Irifune, T., Higo, Y., Inoue, T., Kono, Y., Ohfuji, H., & Funakoshi, K. (2008). Sound velocities
520 of majorite garnet and the composition of the mantle transition region. *Nature*.
521 <https://doi.org/10.1038/nature06551>

522 Kresse, G., & Joubert, D. (1999). From ultrasoft pseudopotentials to the projector augmented-
523 wave method. *Physical Review B - Condensed Matter and Materials Physics*.

524 Kurnosov, A., Marquardt, H., Frost, D. J., Ballaran, T. B., & Ziberna, L. (2017). Evidence for a
525 Fe³⁺-rich pyrolitic lower mantle from (Al,Fe)-bearing bridgmanite elasticity data. *Nature*,
526 13. <https://doi.org/10.1038/nature21390>

527 Li, Y., Vočadlo, L., Brodholt, J., & Wood, I. G. (2016). Thermoelasticity of Fe 7 C 3 under inner
528 core conditions. *Journal of Geophysical Research: Solid Earth*, 121(8), 5828–5837.
529 <https://doi.org/10.1002/2016JB013155>

530 Li, Y., Korzhavyi, P. A., Sandström, R., & Lilja, C. (2017). Impurity effects on the grain
531 boundary cohesion in copper. *PHYSICAL REVIEW MATERIALS*, 1(R), 70602.
532 <https://doi.org/10.1103/PhysRevMaterials.1.070602>

533 Li, Y., Vočadlo, L., & Brodholt, J. P. (2018). The elastic properties of hcp-Fe alloys under the
534 conditions of the Earth's inner core. *Earth and Planetary Science Letters*, 493, 118–127.
535 <https://doi.org/10.1016/j.epsl.2018.04.013>

536 Li, Y., Vočadlo, L., Alfè, D., & Brodholt, J. (2019). Carbon Partitioning Between the Earth's
537 Inner and Outer Core. *Journal of Geophysical Research: Solid Earth*.
538 <https://doi.org/10.1029/2019JB018789>

539 Litasov, K. D., Dorogokupets, P. I., Ohtani, E., Fei, Y., Shatskiy, A., Sharygin, I. S., et al.
540 (2013). Thermal equation of state and thermodynamic properties of molybdenum at high
541 pressures. *Journal of Applied Physics*. <https://doi.org/10.1063/1.4794127>

542 Lord, O. T., Walter, M. J., Dasgupta, R., Walker, D., & Clark, S. M. (2009). Melting in the Fe-C
543 system to 70 GPa. *Earth and Planetary Science Letters*, 284(1–2), 157–167.
544 <https://doi.org/10.1016/j.epsl.2009.04.017>

545 Martorell, B., Vočadlo, L., Brodholt, J., & Wood, I. G. (2013). Strong Premelting Effect in the
546 Elastic Properties of hcp-Fe Under Inner-Core Conditions. *Science*, 342, 466–468.
547 <https://doi.org/10.1126/science.1243651>

- 548 Martorell, B., Brodholt, J., Wood, I. G., & Vočadlo, L. (2013). The effect of nickel on the
549 properties of iron at the conditions of Earth's inner core: Ab initio calculations of seismic
550 wave velocities of Fe-Ni alloys. *Earth and Planetary Science Letters*, 365, 143–151.
551 <https://doi.org/10.1016/j.epsl.2013.01.007>
- 552 Martorell, B., Wood, I. G., Brodholt, J., & Vočadlo, L. (2016). The elastic properties of hcp-Fe
553 $1-x$ Si x at Earth's inner-core conditions. *Earth and Planetary Science Letters*, 451, 89–96.
554 <https://doi.org/10.1016/j.epsl.2016.07.018>
- 555 Mashino, I., Miozzi, F., Hirose, K., Morard, G., & Sinmyo, R. (2019). Melting experiments on
556 the Fe–C binary system up to 255 GPa: Constraints on the carbon content in the Earth's
557 core. *Earth and Planetary Science Letters*, 515, 135–144.
558 <https://doi.org/10.1016/j.epsl.2019.03.020>
- 559 Mezouar, M., Crichton, W. A., Bauchau, S., Thurel, F., Witsch, H., Torrecillas, F., et al. (2005).
560 Development of a new state-of-the-art beamline optimized for monochromatic single-
561 crystal and powder X-ray diffraction under extreme conditions at the ESRF. In *Journal of*
562 *Synchrotron Radiation*. <https://doi.org/10.1107/S0909049505023216>
- 563 Miozzi, F., Matas, J., Guignot, N., Badro, J., Siebert, J., & Fiquet, G. (2020). A new reference
564 for the thermal equation of state of iron. *Minerals*, 10(2).
565 <https://doi.org/10.3390/min10020100>
- 566 Miozzi, F., Morard, G., Antonangeli, D., Baron, M. A., Boccato, S., Pakhomova, A., et al.
567 (2020). Eutectic melting of Fe-3 at% Si-4 at% C up to 200 GPa and implications for the
568 Earth's core. *Earth and Planetary Science Letters*, 544, 116382.
569 <https://doi.org/10.1016/j.epsl.2020.116382>
- 570 Morard, G., Andrault, D., Guignot, N., Siebert, J., Garbarino, G., & Antonangeli, D. (2011).
571 Melting of Fe-Ni-Si and Fe-Ni-S alloys at megabar pressures: Implications for the core-
572 mantle boundary temperature. *Physics and Chemistry of Minerals*.
573 <https://doi.org/10.1007/s00269-011-0449-9>
- 574 Morard, G., Andrault, D., Antonangeli, D., Nakajima, Y., Auzende, A. L., Boulard, E., et al.
575 (2017). Fe–FeO and Fe–Fe₃C melting relations at Earth's core–mantle boundary
576 conditions: Implications for a volatile-rich or oxygen-rich core. *Earth and Planetary*
577 *Science Letters*. <https://doi.org/10.1016/j.epsl.2017.05.024>
- 578 Morard, G., Nakajima, Y., Andrault, D., Antonangeli, D., Auzende, A. L., Boulard, E., et al.
579 (2017). Structure and Density of Fe-C Liquid Alloys Under High Pressure. *Journal of*
580 *Geophysical Research: Solid Earth*. <https://doi.org/10.1002/2017JB014779>
- 581 Murakami, M., Ohishi, Y., Hirao, N., & Hirose, K. (2012). A perovskitic lower mantle inferred
582 from high-pressure, high-temperature sound velocity data. *Nature*, 485(7396), 90–94.
583 <https://doi.org/10.1038/nature11004>
- 584 Pamato, M. G., Kurnosov, A., Boffa Ballaran, T., Frost, D. J., Ziberna, L., Giannini, M., et al.
585 (2016). Single crystal elasticity of majoritic garnets: Stagnant slabs and thermal anomalies
586 at the base of the transition zone. *Earth and Planetary Science Letters*, 451.
587 <https://doi.org/10.1016/j.epsl.2016.07.019>
- 588 Perdew, J. P., & Wang, Y. (1992). Accurate and simple analytic representation of the electron-
589 gas correlation energy. *Physical Review B*. <https://doi.org/10.1103/PhysRevB.45.13244>

590 Prescher, C., & Prakapenka, V. B. (2015). DIOPTAS: A program for reduction of two-
591 dimensional X-ray diffraction data and data exploration. *High Pressure Research*.
592 <https://doi.org/10.1080/08957959.2015.1059835>

593 Prescher, C., Dubrovinsky, L., Bykova, E., Kuppenko, I., Glazyrin, K., Kantor, A., et al. (2015).
594 High Poisson's ratio of Earth's inner core explained by carbon alloying. *Nature Geoscience*.
595 <https://doi.org/10.1038/ngeo2370>

596 Ross, R. G., & Hume-Rothery, W. (1963). High temperature X-ray metallography. I. A new
597 debye-scherrer camera for use at very high temperatures II. A new para-focusing camera III.
598 Applications to the study of chromium, hafnium, molybdenum, rhodium, ruthenium and
599 tungsten. *Journal of The Less-Common Metals*. [https://doi.org/10.1016/0022-](https://doi.org/10.1016/0022-5088(63)90031-6)
600 [5088\(63\)90031-6](https://doi.org/10.1016/0022-5088(63)90031-6)

601 Sakai, T., Takahashi, S., Nishitani, N., Mashino, I., Ohtani, E., & Hirao, N. (2014). Equation of
602 state of pure iron and Fe_{0.9}Ni_{0.1} alloy up to 3 Mbar. *Physics of the Earth and Planetary*
603 *Interiors*, 228, 114–126. <https://doi.org/10.1016/J.PEPI.2013.12.010>

604 Shahar, A., Ziegler, K., Young, E. D., Ricolleau, A., Schauble, E. A., & Fei, Y. (2009).
605 Experimentally determined Si isotope fractionation between silicate and Fe metal and
606 implications for Earth's core formation. *Earth and Planetary Science Letters*.
607 <https://doi.org/10.1016/j.epsl.2009.09.025>

608 Siebert, J., Badro, J., Antonangeli, D., & Ryerson, F. J. (2013). Terrestrial accretion under
609 oxidizing conditions. *Science*. <https://doi.org/10.1126/science.1227923>

610 Smidt, F. A., & Sprague, J. A. (1972). PROPERTY CHANGES RESULTING FROM
611 IMPURITY-DEFECT INTERACTIONS IN IRON AND PRESSURE VESSEL STEEL
612 ALLOYS. In *ASTM Special Technical Publication*.

613 Vočadlo, L. (2007). Ab initio calculations of the elasticity of iron and iron alloys at inner core
614 conditions: Evidence for a partially molten inner core? *Earth and Planetary Science Letters*,
615 254(1–2), 227–232. <https://doi.org/10.1016/j.epsl.2006.09.046>

616 Waseda, Y., Matsubara, E., & Shinoda, K. (2011). *X-Ray Diffraction Crystallography*. Springer
617 Berlin Heidelberg. <https://doi.org/10.1007/978-3-642-16635-8>

618 Yang, J., Fei, Y., Hu, X., Greenberg, E., & Prakapenka, V. (2019). Effect of Carbon on the
619 Volume of Solid Iron at High Pressure: Implications for Carbon Substitution in Iron
620 Structures and Carbon Content in the Earth's Inner Core. *Minerals*, 9(12), 720.
621 <https://doi.org/10.3390/min9120720>

622

623

624

625

626

627

628

629
630
631
632
633
634
635
636
637

Table 1. EoS parameters of *hcp* Fe alloys

| V_0 (\AA^3) | K_0 (GPa) | K' | composition | Reference |
|--------------------------|-------------|----------|--|---|
| <i>experiments</i> | | | | |
| 22.7(2) | 148(18) | 5.8(4) | Fe-4 at% C-3 at% Si | This study |
| 22.524(62) | 172.4(6.0) | 4.64(14) | Fe-8 at% Si | Edmund et al. (2019) |
| 22.5(1) | 170(10) | 4.7(2) | Fe-8 at% Si | Edmund et al. (2019) (our fit) |
| 22.37(4) | 168.9(4.8) | 5.18(14) | Fe-1.4 at% C | Yang et al. (2019) |
| 22.40(6) | 164(8) | 5.4(3) | Fe-1.4 at% C | Yang et al. (2019) (our fit) |
| 22.37(6) | 182.2(4.2) | 4.68(17) | Fe-6.1 at% C | Yang et al. (2019) |
| 22.44(5) | 174(6) | 4.88(18) | Fe-6.1 at% C | Yang et al. (2019) (our fit) |
| 22.26(6) | 169.7(5.2) | 5.19(16) | Fe | Yang et al. (2019) |
| 22.32(5) | 163(5) | 5.36(5) | Fe | Yang et al. (2019) (our fit) |
| 22.468(24) | 165(fixed) | 4.97(4) | Fe | Dewaele et al. (2006) |
| 22.31(8) | 178(7) | 4.75(12) | Fe | Dewaele et al. (2006) (our fit) |
| 22.80(2) | 129(6) | 6.2(2) | Fe | Miozzi, Matas, et al. (2020) |
| 22.80(7) | 130(6) | 6.2(2) | Fe | Miozzi, Matas, et al. (2020) (our fit) |
| 22.468 (fixed) | 155.3(2.2) | 5.37(14) | Fe | Sakai et al. (2014) |
| 22.5(2) | 151(15) | 5.5(4) | Fe | Sakai et al. (2014) (our fit) |
| <i>calculations</i> | | | | |
| 20.40 | 281 | 4.4 | $\text{Fe}_{60}\text{C}_2^{\text{s}}\text{Si}_2$ | This study |
| 20.85 | 305 | 4.3 | $\text{Fe}_{62}\text{C}_2^{\text{i}}\text{Si}_2$ | This study |
| 20.39 | 313 | 4.3 | $\text{Fe}_{61}\text{C}_2^{\text{d}}\text{Si}_2$ | This study |
| 21.46 | 291 | 4.34 | Fe-6 at% C ⁱ | Huang et al. (2005) |
| 20.29 | 312 | 4.3 | Fe | This study |

^s substitutional C, ⁱ interstitial C, ^d dimer C

638

639 **Figure Captions**

640

641 **Figure 1.** Angle-dispersive x-ray powder diffraction pattern of *hcp* Fe-C-Si alloy (+ Ne)
642 collected at ~140 GPa and 300 K. The reflection positions of Neon (orange) and Fe-C-Si alloy
643 (grey) are shown by the tick markers.

644 **Figure 2.** a) Unit-cell volume of Fe-C-Si alloy as a function of pressure. Error bars are smaller
645 than symbols. Lines correspond to the fit of the data to a third-order Birch-Murnaghan equation
646 of state. Literature data for Fe-alloys (Edmund et al., 2019; Yang et al., 2019) and reference EoS
647 for pure Fe (Dewaele et al., 2006; Sakai et al., 2014; Yang et al., 2019; Miozzi, Matas, et al.,
648 2020) are shown for comparison. Inset: confidence ellipses centred on each data point,
649 representing the 68.3% confidence level. The reported 1σ error bars for K_0 and K_0' were derived
650 from least-squares refinements. b) Unit-cell volumes of Fe-C alloys showing effect of C in the
651 unit cell volume of *hcp* Fe.

652 **Figure 3.** Calculated enthalpy of carbon (referenced to the isolated atom) in the form of
653 substitutional, interstitial and dimer defects in the *hcp* Fe-C alloy at 0 K.

654 **Figure 4.** Calculated and measured unit-cell volumes of Fe-C-Si alloys with pressure showing
655 the effect of different incorporation mechanisms of C in the alloy structure. The solid lines are
656 the fit of the data to a third-order Birch-Murnaghan EoS. The red solid line corresponds to the
657 EoS of Fe calculated in this study.

658 **Figure 5.** Comparison between calculations and experiments for *hcp* Fe and Fe-C-Si alloys as a
659 function of pressure.

660 **Figure 6.** Volume variation, $\Delta V = V - V_{\text{Fe}}$ (where V is the unit-cell volume of the alloy and V_{Fe} is
661 the reference unit-cell volume for *hcp* Fe) for *hcp* Fe alloys as a function of pressure. For the

662 experimental results from the present work different reference EoS for pure Fe (Dewaele et al.,
663 2006; Sakai et al., 2014; Yang et al., 2019; Miozzi, Matas, et al., 2020) were taken from the
664 literature. The calculated volumes of $\text{Fe}_{62}\text{C}_2\text{Si}_2$ (C interstitial), $\text{Fe}_{61}\text{C}_2\text{Si}_2$ (dimer) and $\text{Fe}_{60}\text{C}_2\text{Si}_2$
665 (substitutional) are normalized to *hcp* Fe from our DFT simulations.

666 **Figure 7.** Density evolution with pressure for different *hcp* Fe-C-Si alloys. Solid lines represent
667 densities calculated considering C as interstitial, whereas dashed lines are densities calculated
668 assuming C as substitutional, starting from the same volumes.

669 **Figure 8.** Density variation with pressure for different *hcp* Fe-C-Si alloys calculated at 300 K
670 (experiments) and 0 K (DFT calculations). Dashed lines represent density calculated considering
671 C as substitutional, solid lines are densities calculated assuming C as interstitial and dotted lines
672 are densities calculated with C as a dimer. For simplicity, only recent data for pure Fe from Yang
673 et al. (2019) are shown as reference. The DFT calculations, in which both the changes in unit-
674 cell volume and unit-cell contents are taken into account in an internally consistent way, show
675 that the density difference between a substitutional, interstitial and dimer alloy is almost
676 negligible. In the case of the experiments, the volume is directly measured, without any *a priori*
677 assumption of C distribution and assumptions of effective mass of the unit-cell have to be made
678 to derive density from the measured volumes. If the experimental results are interpreted
679 incorrectly as substitutional, then it would erroneously predict much lower densities.

680

681

682

683

Figure 1.

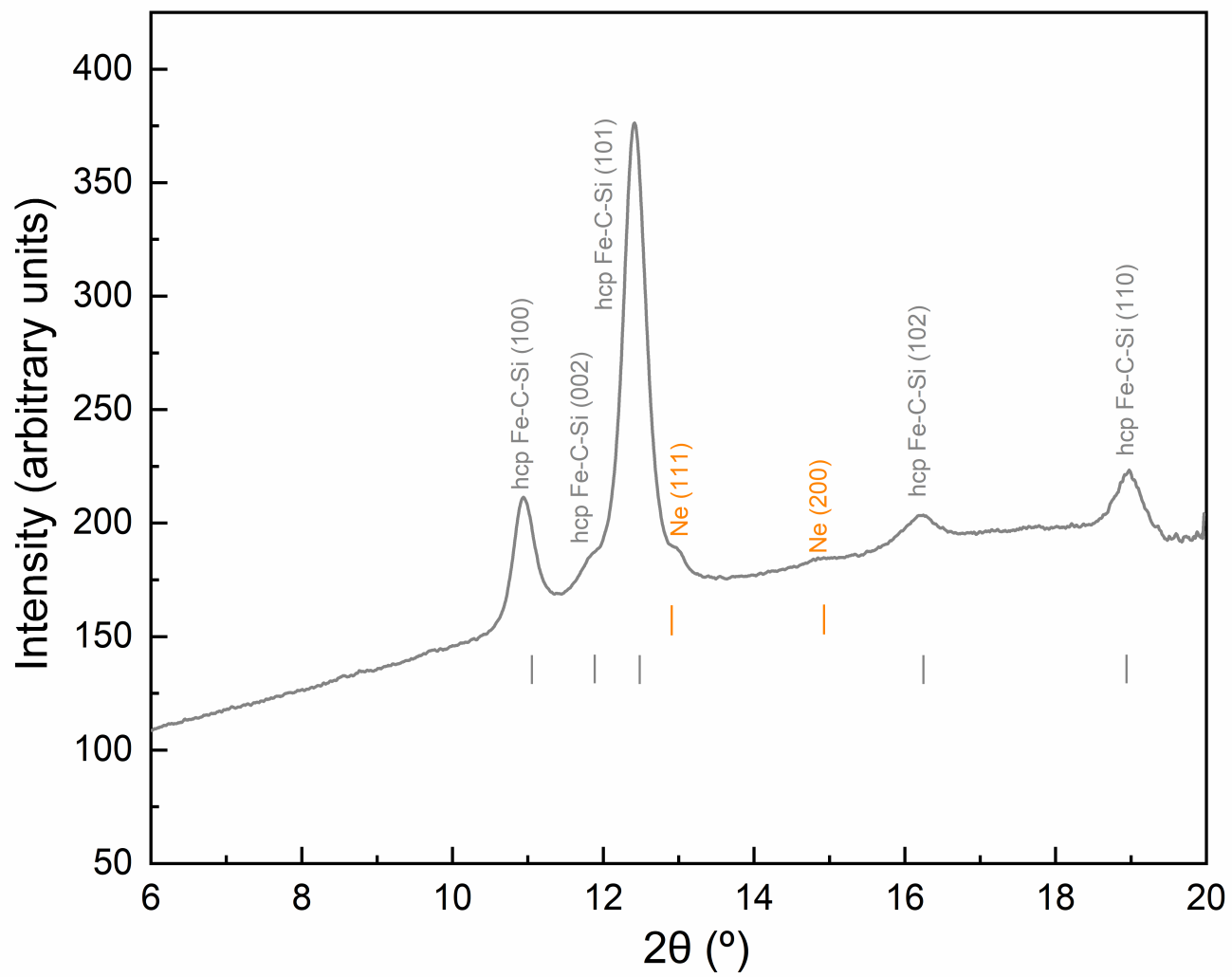


Figure 2.

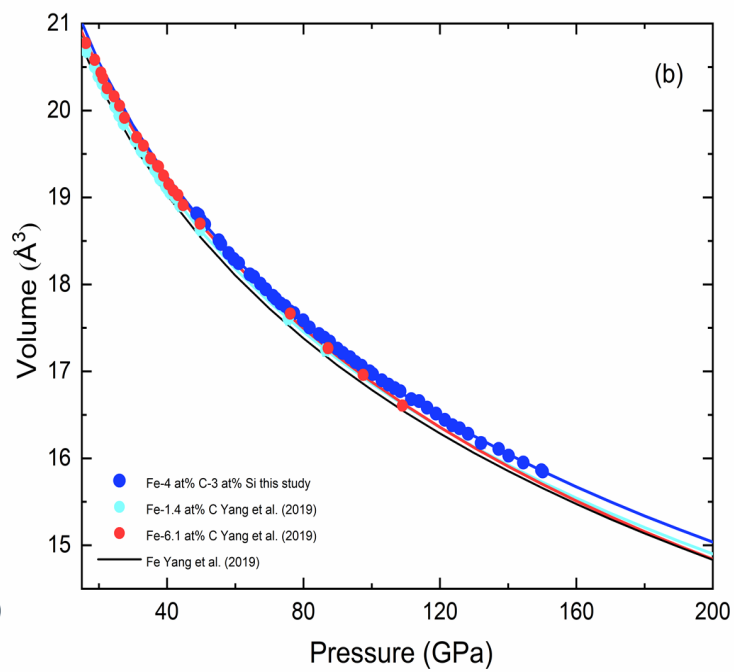
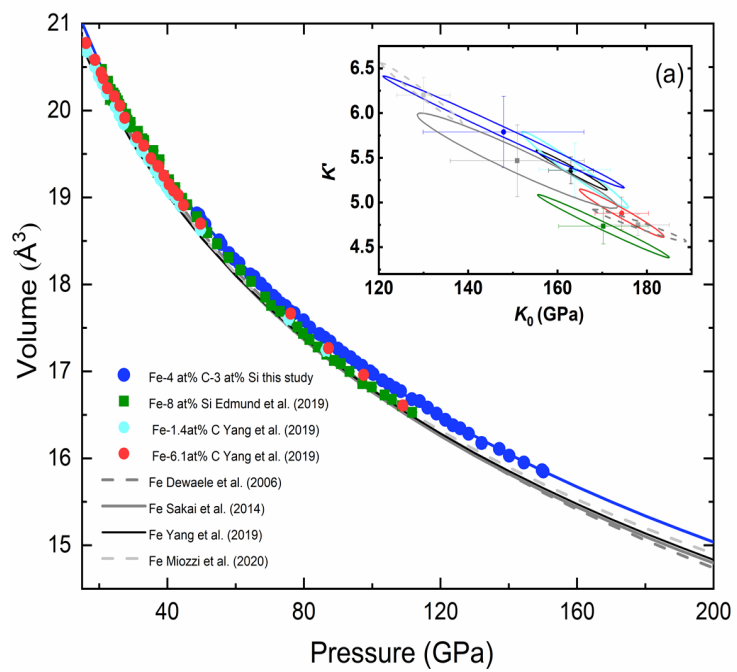


Figure 3.

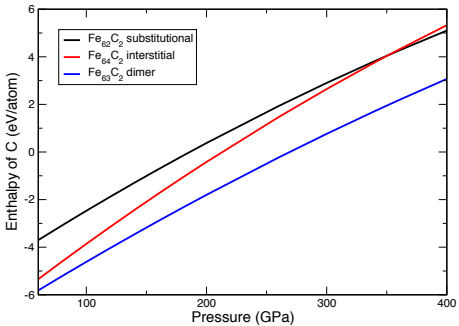


Figure 4.

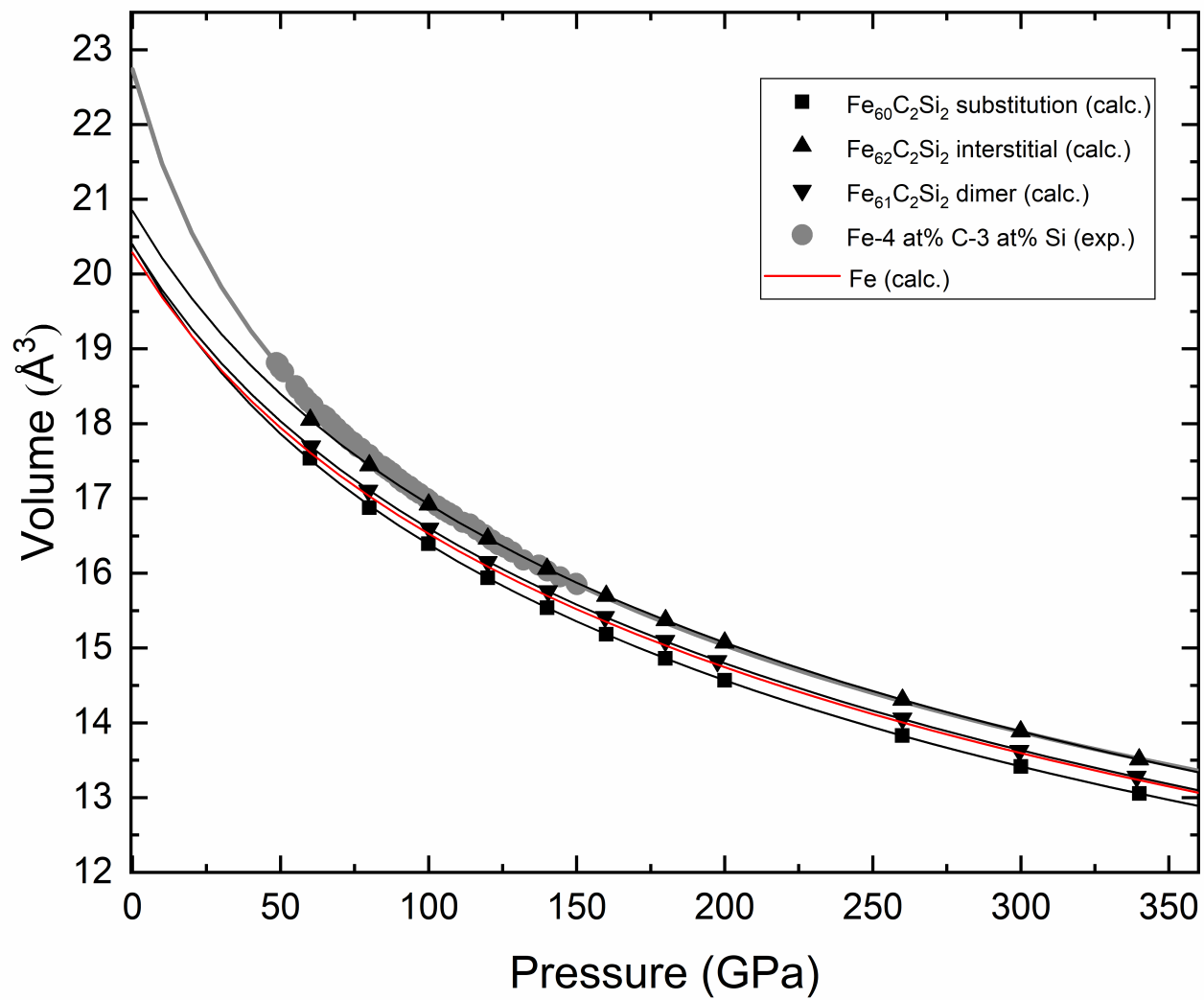


Figure 5.

Figure 6.

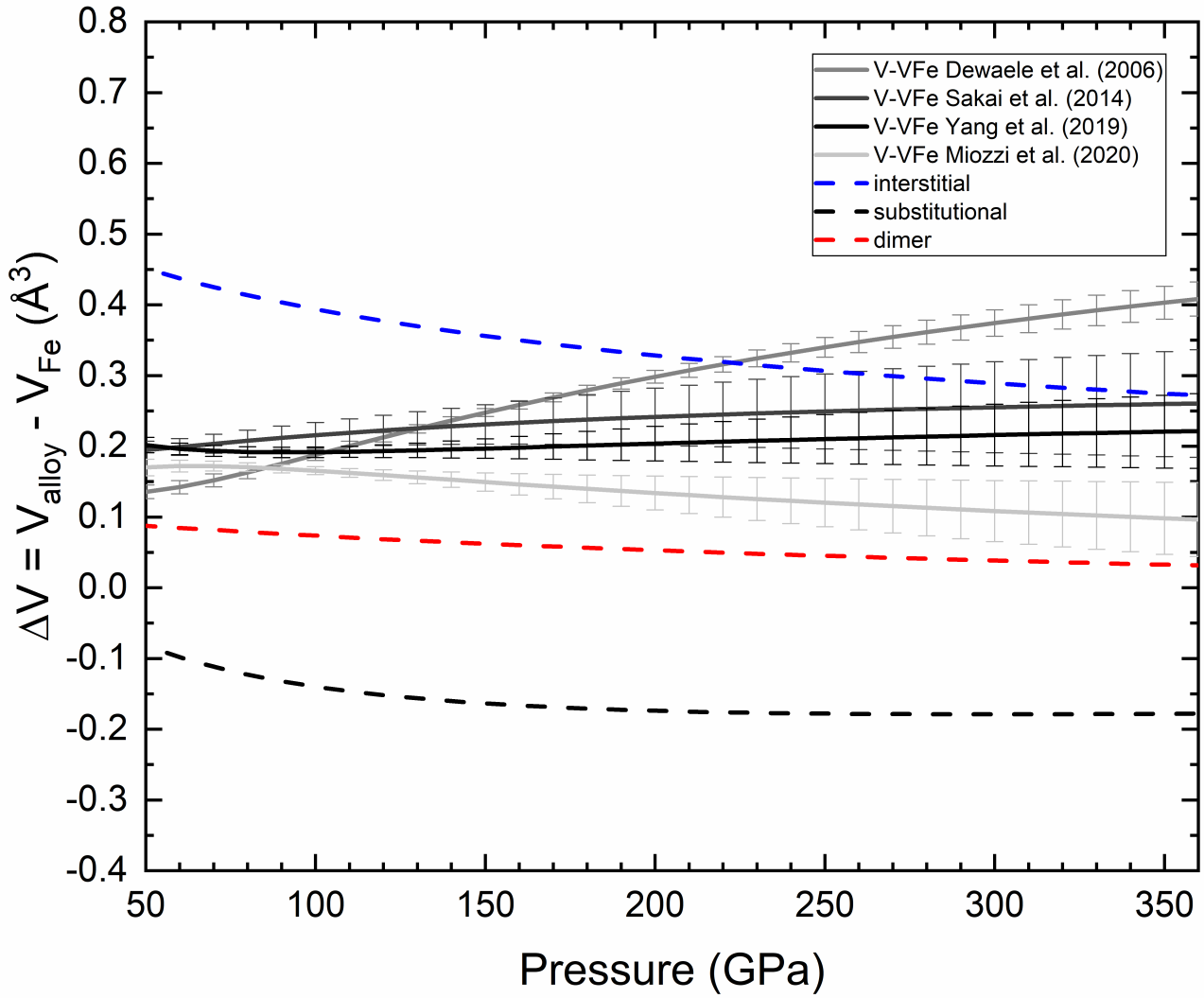


Figure 7.

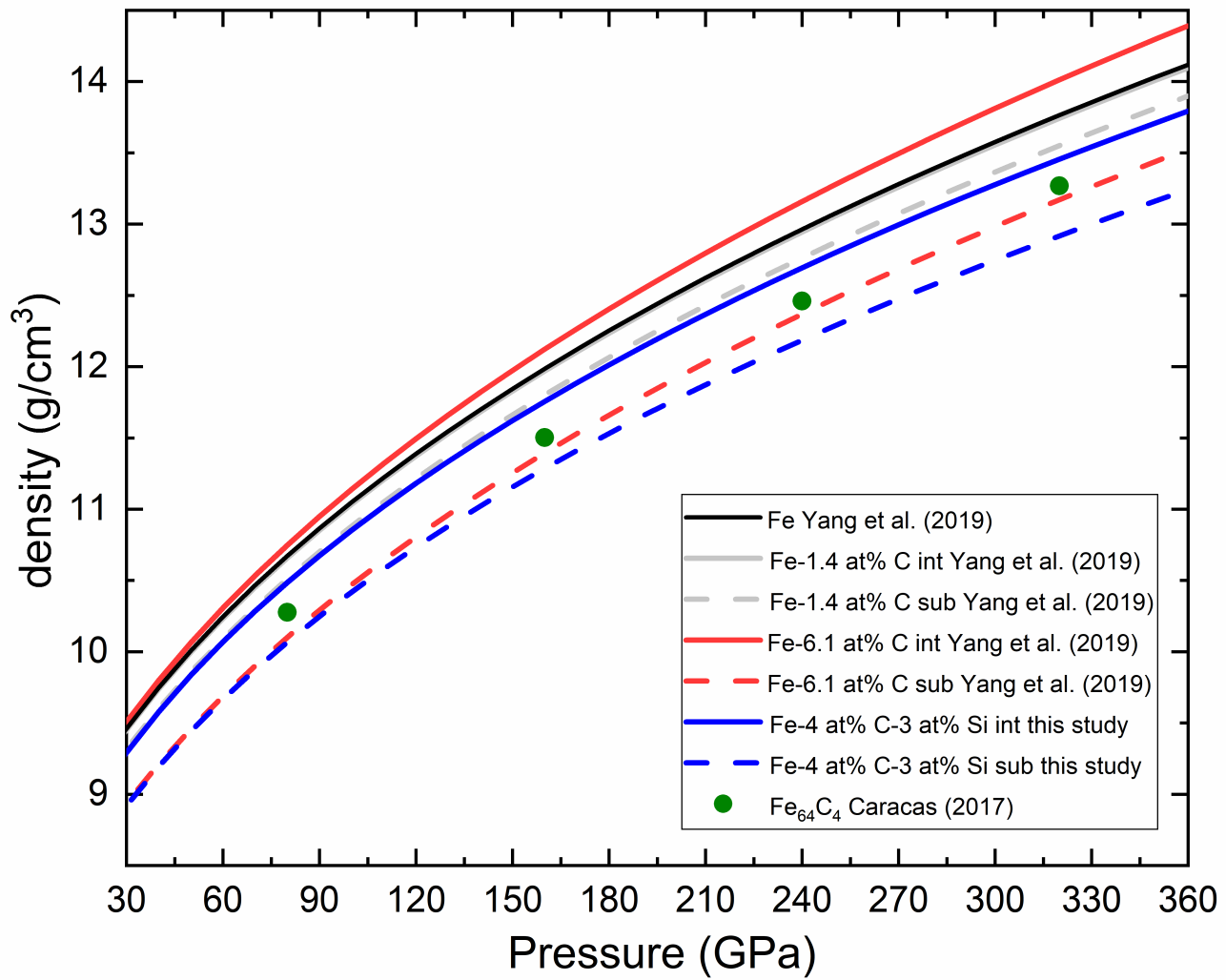
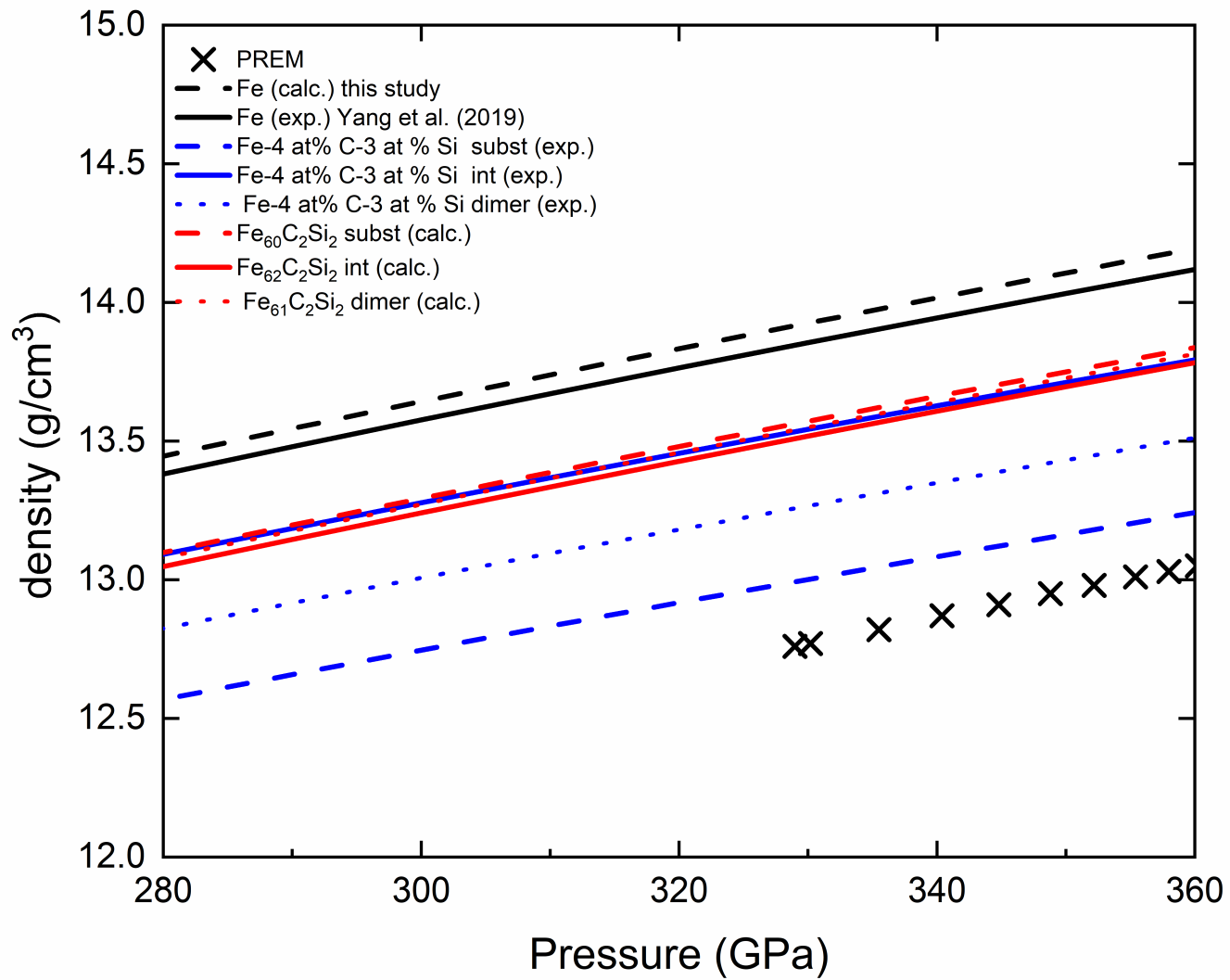


Figure 8.



Supporting Information for

Equation of State of *hcp* Fe-C-Si Alloys and the Effect of C Incorporation Mechanism on the Density of *hcp* Fe alloys at 300 K

M.G. Pamato^{1,2*}, Y. Li¹, D. Antonangeli³, F. Miozzi^{3†}, G. Morard^{3,4}, I.G. Wood¹, L. Vočadlo¹, J.P. Brodholt¹, M. Mezouar⁵

¹ Department of Earth Sciences, University College London, Gower Street, London, WC1E 6BT, United Kingdom, ² Department of Geosciences, University of Padova, Via G. Gradenigo 6, 35131, Padova, Italy, ³ Sorbonne Université, Muséum National d' Histoire Naturelle, UMR CNRS 7590, Institut de Minéralogie, de Physique des Matériaux, et de Cosmochimie (IMPMC), 75005 Paris, France, ⁴ Univ. Grenoble Alpes, Univ. Savoie Mont Blanc, CNRS, IRD, IFSTTAR, ISTerre, 38000 Grenoble, France, ⁵ European Synchrotron Radiation Facility, Grenoble, France *

Corresponding author: Martha G. Pamato (martha.pamato@unipd.it)

† Current address: Dipartimento di Scienze della Terra, Università degli Studi di Milano, via Mangiagalli 34, 20133 Milano, Italy.

Contents of this file

Text S1
Figure S1 to S2
Tables S1 to S3
Tables S4 (File uploaded separately)

Introduction

These supplemental materials include: Figure S1, showing details of the different configurations of C in *hcp* Fe; Figure S2, showing the effect of interstitial C on the volume of *hcp* Fe; Text S1, describing the density calculations for different alloys: substitutional, interstitial and dimer; Tables S1 and S2, reporting unit cell parameters and density of *hcp* Fe-Si-C from experiments and calculations, respectively; Table S3, summarizing the results from enthalpy calculations; Table S4 (uploaded separately) reporting the resulting stress matrices.

Text S1.

As reported in the main text, we denote the alloy with both substitutional and interstitial solute elements as $A_{1-x-y}B_x^S C_y^I$, where A is the solid solvent, B and C are the substitutional and interstitial solutes, respectively. x and y are the molar fraction. The density of the alloy can be calculated by

$$\rho = \frac{N \cdot \left[\left(\frac{1-x-y}{1-y} \right) \cdot M_A + \frac{x}{1-y} \cdot M_B + \frac{y}{1-y} M_C \right]}{V}$$

where N is the number of atoms in unit cell, and it is two for the *hcp* structure. V is the volume of unit cell. M_A , M_B and M_C are the molar mass for A, B and C respectively.

In the case of Fe- 4 at% C and 3 at% Si investigated in this study, the density at $P= 48.8$ GPa, $V = 18.816 \text{ \AA}^3$ (see Table S1) is calculated:

$$\rho = \frac{2 \cdot \left[\left(\frac{1 - 0.03 - 0.04}{1 - 0.04} \right) \cdot 55.845 + \frac{0.03}{1 - 0.04} \cdot 28.085 + \frac{0.04}{1 - 0.04} \cdot 12.011 \right]}{11.331}$$

$$\rho = 9.792 \text{ g/cm}^3$$

Where $V = 18.816 \times 10^{-24} \times 6.022 \times 10^{23} = 11.331 \text{ cm}^3$

The density calculations for other alloys can be derived from the equation above. If both B and C are substitutional, the density for $A_{1-x-y}B_x^S C_y^S$ is then:

$$\rho = \frac{N \cdot [(1-x-y) \cdot M_A + x \cdot M_B + y \cdot M_C]}{V}$$

In the case of Fe- 4 at% C and 3 at% Si investigated in this study, the density at $P= 48.8$ GPa, $V = 18.816 \text{ \AA}^3$ (see Table S1) is calculated:

$$\rho = 2 \cdot [(1 - 0.03 - 0.04) \cdot 55.845 + 0.03 \cdot 28.085 + 0.04 \cdot 12.011] / 11.331$$

$$\rho = 9.400 \text{ g/cm}^3$$

If both B and C are interstitial, the density for $A_{1-x-y}B_x^I C_y^I$ is then

$$\rho = N \cdot \left[M_A + \frac{x}{1-x-y} M_B + \frac{y}{1-x-y} M_C \right] / V$$

The dimer defect with two C atoms sitting at one lattice site is actually also a combination of one substitutional and one interstitial C.

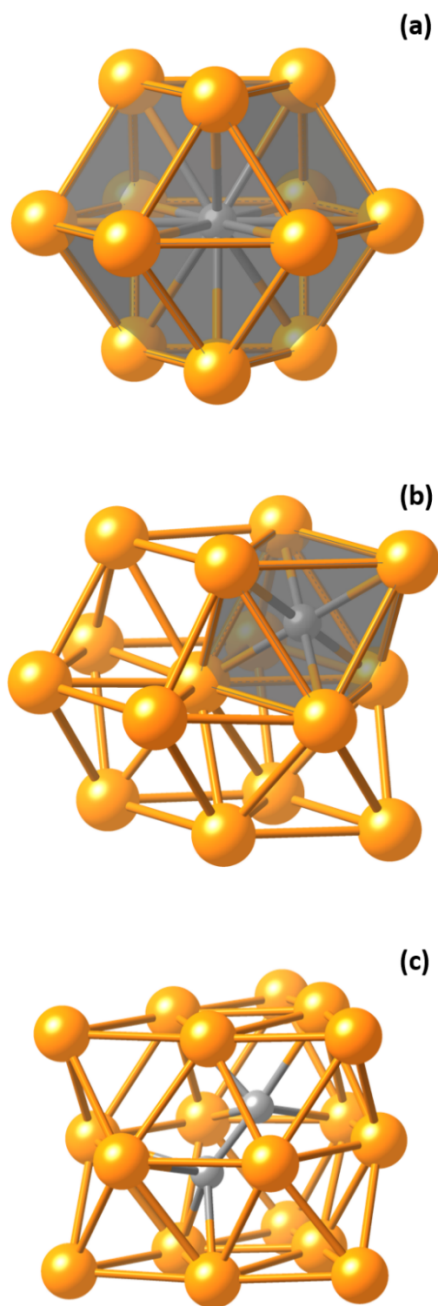


Figure S1. Illustration of the different configurations of C in *hcp* Fe. (a) substitutional; (b) octahedral interstitial site; (c) 2 C atoms occupying one atomic site (dimer defect)

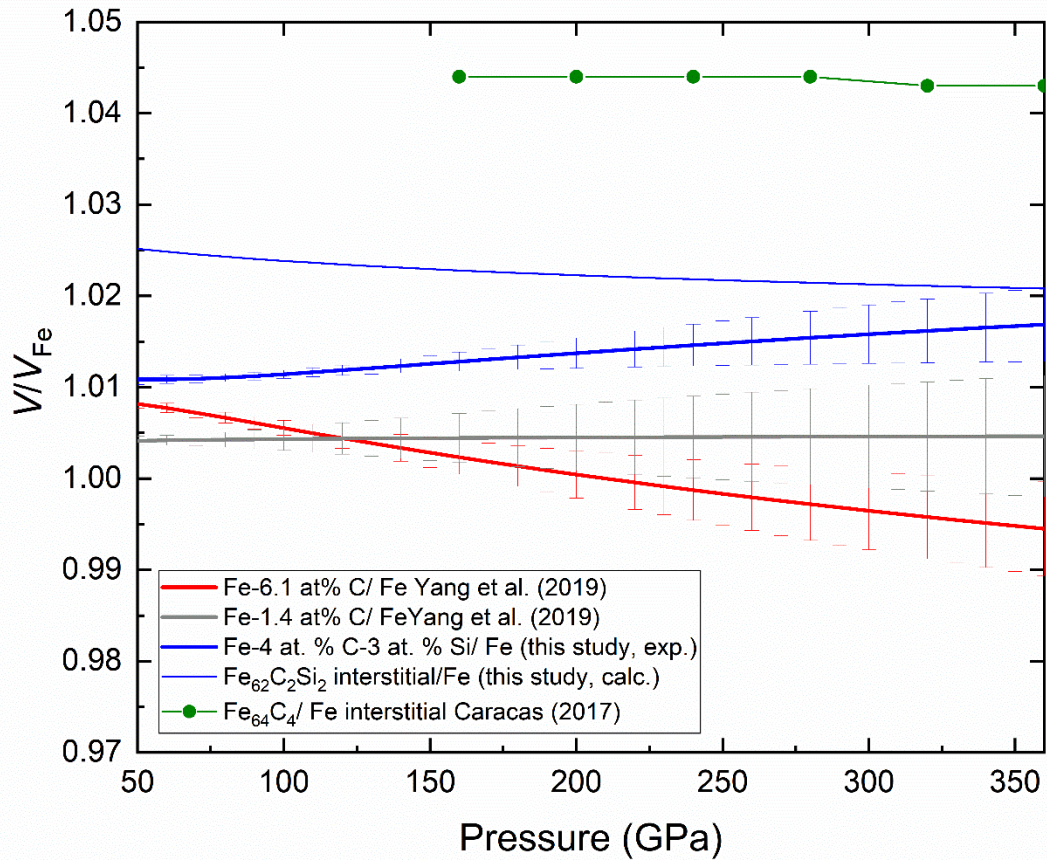


Figure S2. Pressure dependence of the volume ratio V/V_{Fe} (where V is the unit-cell volume of the alloy and V_{Fe} is the reference unit-cell volume for *hcp* Fe) for *hcp* Fe and Fe-Si alloys with different amounts of C. For all of the experimental results, i.e. those from the present work and those from Yang et al. (2019), the reference V_{Fe} was taken from Yang et al. (2019). In addition, the calculated volumes of $\text{Fe}_{62}\text{C}_2\text{Si}_2$ (C interstitial) normalized to *hcp* Fe from our DFT simulations, are also plotted, as are the results for Fe_{64}C_4 (~6 at% C) by Caracas (2017).

| P(GPa) | $V(\text{\AA}^3)$ | $a(\text{\AA})$ | $c(\text{\AA})$ | $\rho(\text{g/cm}^3)^{\text{int}}$ | $\rho(\text{g/cm}^3)^{\text{sub.}}$ | $\rho(\text{g/cm}^3)^{\text{dimer}}$ |
|---------|-------------------|-----------------|-----------------|------------------------------------|-------------------------------------|--------------------------------------|
| 48.6(4) | 18.816(11) | 2.388(3) | 3.812(15) | 9.792 | 9.400 | 9.592 |

| | | | | | | |
|-----------|------------|----------|-----------|--------|--------|--------|
| 49.3(4) | 18.799(11) | 2.387(3) | 3.811(14) | 9.801 | 9.409 | 9.601 |
| 49.9(5) | 18.742(11) | 2.385(3) | 3.805(15) | 9.831 | 9.437 | 9.630 |
| 51.1(4) | 18.691(11) | 2.383(3) | 3.802(14) | 9.858 | 9.463 | 9.656 |
| 55.2(5) | 18.507(11) | 2.375(3) | 3.788(14) | 9.956 | 9.557 | 9.753 |
| 55.8(5) | 18.464(11) | 2.373(3) | 3.785(14) | 9.979 | 9.580 | 9.775 |
| 58.0(5) | 18.359(11) | 2.369(3) | 3.777(14) | 10.036 | 9.634 | 9.831 |
| 59.6(6) | 18.291(11) | 2.366(3) | 3.772(14) | 10.073 | 9.670 | 9.868 |
| 61.0(6) | 18.244(11) | 2.364(3) | 3.769(13) | 10.099 | 9.695 | 9.893 |
| 64.3(4) | 18.115(11) | 2.360(4) | 3.756(16) | 10.171 | 9.764 | 9.963 |
| 65.4(4) | 18.088(11) | 2.358(4) | 3.757(15) | 10.186 | 9.779 | 9.978 |
| 67.4(5) | 18.009(11) | 2.355(4) | 3.749(16) | 10.231 | 9.822 | 10.022 |
| 69.0(5) | 17.944(11) | 2.352(4) | 3.744(17) | 10.268 | 9.857 | 10.058 |
| 71.0(4) | 17.868(11) | 2.349(4) | 3.738(17) | 10.312 | 9.899 | 10.101 |
| 71.9(5) | 17.836(11) | 2.348(4) | 3.737(17) | 10.330 | 9.917 | 10.119 |
| 73.3(5) | 17.780(11) | 2.346(4) | 3.730(17) | 10.363 | 9.948 | 10.151 |
| 74.6(5) | 17.750(11) | 2.344(4) | 3.730(16) | 10.380 | 9.965 | 10.168 |
| 76.0(5) | 17.691(11) | 2.342(4) | 3.725(16) | 10.415 | 9.998 | 10.202 |
| 77.2(5) | 17.670(11) | 2.340(4) | 3.725(15) | 10.427 | 10.010 | 10.214 |
| 79.9(5) | 17.587(10) | 2.336(4) | 3.720(16) | 10.476 | 10.057 | 10.262 |
| 81.8(5) | 17.505(10) | 2.334(4) | 3.709(17) | 10.525 | 10.104 | 10.310 |
| 84.6(6) | 17.429(10) | 2.330(4) | 3.707(16) | 10.571 | 10.148 | 10.355 |
| 86.1(6) | 17.387(10) | 2.328(3) | 3.703(15) | 10.597 | 10.173 | 10.381 |
| 87.7(7) | 17.343(10) | 2.326(3) | 3.702(14) | 10.624 | 10.199 | 10.407 |
| 90.0(7) | 17.262(10) | 2.322(3) | 3.696(15) | 10.674 | 10.247 | 10.455 |
| 91.6(8) | 17.211(10) | 2.320(3) | 3.691(15) | 10.705 | 10.277 | 10.487 |
| 93.7(8) | 17.162(10) | 2.317(3) | 3.690(14) | 10.736 | 10.306 | 10.517 |
| 95.2(8) | 17.107(10) | 2.316(3) | 3.683(14) | 10.770 | 10.339 | 10.551 |
| 97.0(7) | 17.064(10) | 2.313(3) | 3.683(14) | 10.797 | 10.365 | 10.577 |
| 99.4(7) | 17.000(10) | 2.310(3) | 3.679(13) | 10.838 | 10.405 | 10.617 |
| 100.3(7) | 16.969(10) | 2.309(3) | 3.675(13) | 10.858 | 10.424 | 10.636 |
| 103.0(7) | 16.898(10) | 2.305(3) | 3.672(13) | 10.903 | 10.467 | 10.681 |
| 105.0(6) | 16.848(10) | 2.303(3) | 3.668(14) | 10.936 | 10.498 | 10.713 |
| 106.7(6) | 16.808(10) | 2.302(3) | 3.664(15) | 10.962 | 10.523 | 10.738 |
| 108.3(6) | 16.772(10) | 2.299(3) | 3.663(14) | 10.985 | 10.546 | 10.761 |
| 111.6(6) | 16.680(10) | 2.295(3) | 3.656(13) | 11.046 | 10.604 | 10.821 |
| 113.9(7) | 16.659(10) | 2.294(3) | 3.656(12) | 11.061 | 10.618 | 10.834 |
| 116.3(8) | 16.583(10) | 2.291(3) | 3.649(13) | 11.111 | 10.666 | 10.884 |
| 118.9(8) | 16.515(10) | 2.289(3) | 3.641(12) | 11.156 | 10.710 | 10.929 |
| 121.4(9) | 16.443(10) | 2.286(3) | 3.633(13) | 11.205 | 10.757 | 10.976 |
| 123.7(10) | 16.380(9) | 2.283(3) | 3.628(13) | 11.248 | 10.798 | 11.019 |
| 125.8(10) | 16.345(9) | 2.281(3) | 3.626(12) | 11.272 | 10.821 | 11.043 |
| 128.3(9) | 16.283(9) | 2.279(3) | 3.619(12) | 11.315 | 10.863 | 11.085 |
| 132.0(12) | 16.176(9) | 2.275(3) | 3.609(12) | 11.390 | 10.935 | 11.157 |
| 137.2(10) | 16.108(9) | 2.271(3) | 3.606(12) | 11.438 | 10.981 | 11.205 |
| 140.2(10) | 16.030(9) | 2.268(3) | 3.598(12) | 11.494 | 11.034 | 11.260 |
| 144.4(10) | 15.952(9) | 2.266(3) | 3.586(13) | 11.550 | 11.088 | 11.315 |
| 149.8(10) | 15.863(9) | 2.263(3) | 3.576(15) | 11.615 | 11.150 | 11.378 |
| 150.1(9) | 15.848(9) | 2.262(3) | 3.575(14) | 11.626 | 11.161 | 11.389 |

Table S1. Experimental lattice parameters and resulting densities of Fe-C-Si alloy

| Fe | | Fe ₆₀ C ₂ Si ₂ substitutional | | | Fe ₆₂ C ₂ Si ₂ interstitial | | | Fe ₆₁ C ₂ Si ₂ dimer | | | |
|------------|------------------------|--|------------|------------------------|--|------------|--------------------|---|-----------|--------------------|------------|
| P (GPa) | V (Å ³) | ρ (g/cm ³) | P (GPa) | V (Å ³) | ρ (g/cm ³) | P (GPa) | V(Å ³) | ρ (g/cm ³) | P (GP) | V(Å ³) | ρ (g/c) |

|) |) |) |) |) |) |) |) |) | a) | m ³) | |
|-----|-------|-------|-------|-------|--------|-------|------|-------|---------|------------------|--------|
| 60 | 17.61 | 10.52 | 59.98 | 17.53 | 10.153 | 60.01 | 18.0 | 10.18 | 60.33 | 17.69 | 10.224 |
| | 7 | 8 | 3 | 5 | | 1 | 53 | 3 | | 7 | |
| 80 | 17.02 | 10.89 | 80.00 | 16.87 | 10.549 | 80.00 | 17.4 | 10.53 | 79.702 | 17.10 | 10.578 |
| | 9 | 1 | 3 | 7 | | 1 | 42 | 9 | | 4 | |
| 100 | 16.52 | 11.22 | 99.98 | 16.39 | 10.859 | 100.0 | 16.9 | 10.86 | 100.254 | 16.59 | 10.903 |
| | 2 | 5 | 7 | 5 | | 1 | 19 | 5 | | 5 | |
| 120 | 16.08 | | | 15.93 | 11.171 | 119.9 | 16.4 | 11.16 | 119.975 | 16.15 | 11.481 |
| | 6 | 11.53 | 120 | 7 | | 9 | 63 | 6 | | 1 | |
| 140 | 15.69 | 11.81 | | 15.53 | 11.459 | 140.0 | 16.0 | 11.44 | 140.389 | 15.76 | 11.737 |
| | 8 | 5 | 140 | 7 | | 1 | 60 | 7 | | 0 | |
| 160 | 15.34 | 12.08 | 159.9 | 15.18 | 11.726 | | 15.6 | 11.71 | 159.567 | 15.41 | 11.987 |
| | 9 | 4 | 8 | 3 | | 160 | 98 | 1 | | 5 | |
| 180 | 15.03 | 12.33 | 179.9 | 14.86 | 11.98 | | 15.3 | | 179.979 | 15.09 | 12.205 |
| | 2 | 8 | 9 | 2 | | 180 | 71 | 11.96 | | 5 | |
| 200 | 14.74 | | | 14.57 | 12.22 | | 15.0 | 12.19 | 197.562 | 14.82 | 12.87 |
| | 3 | 12.58 | 200 | 0 | | 200 | 72 | 7 | | 5 | |
| 260 | 14.00 | 13.24 | 259.9 | 13.82 | 12.875 | 260.0 | 14.3 | 12.84 | 260.014 | 14.05 | 11.203 |
| | 8 | 1 | 9 | 8 | | 1 | 09 | 7 | | 8 | |
| 300 | 13.59 | 13.64 | 300.0 | 13.41 | 13.271 | 299.9 | 13.8 | | 299.51 | 13.62 | 13.279 |
| | 6 | 1 | 1 | 6 | | 9 | 85 | 13.24 | | 6 | |
| 340 | 13.23 | 14.01 | | 13.05 | 13.639 | 339.9 | 13.5 | 13.60 | 339.157 | 13.27 | 13.627 |
| | 1 | 8 | 340 | 3 | | 9 | 09 | 8 | | 8 | |

Table S2. Volumes and densities of *hcp* Fe and Fe-C-Si alloys from DFT calculations.

| P (GPa) | Enthalpy (eV/atom) | | |
|---------|---------------------------------|---------------------------------|---------------------------------|
| | Fe ₆₂ C ₂ | Fe ₆₄ C ₂ | Fe ₆₃ C ₂ |
| 60 | -3.68 | -5.39 | -5.85 |
| 80 | -3.05 | -4.59 | -5.22 |
| 100 | -2.48 | -3.77 | -4.53 |
| 120 | -1.92 | -3.14 | -4.10 |
| 140 | -1.20 | -2.39 | -3.40 |
| 160 | -0.79 | -1.77 | -2.93 |
| 180 | -0.27 | -1.14 | -2.26 |
| 200 | 0.37 | -0.47 | -1.85 |
| 260 | 2.00 | 1.36 | -0.35 |
| 300 | 3.01 | 2.77 | 0.93 |
| 340 | 3.81 | 3.90 | 1.66 |
| 360 | 4.18 | 4.24 | 2.13 |
| 400 | 5.11 | 5.27 | 3.11 |

Table S3. Enthalpy calculations for the different alloys